A Characterization Method for Hard-Soft Material Interfaces in Structural Optimization

Paul van Houten

Delft University of Technology
BioMechanical Engineering
Biomaterials & Tissue Biomechanics

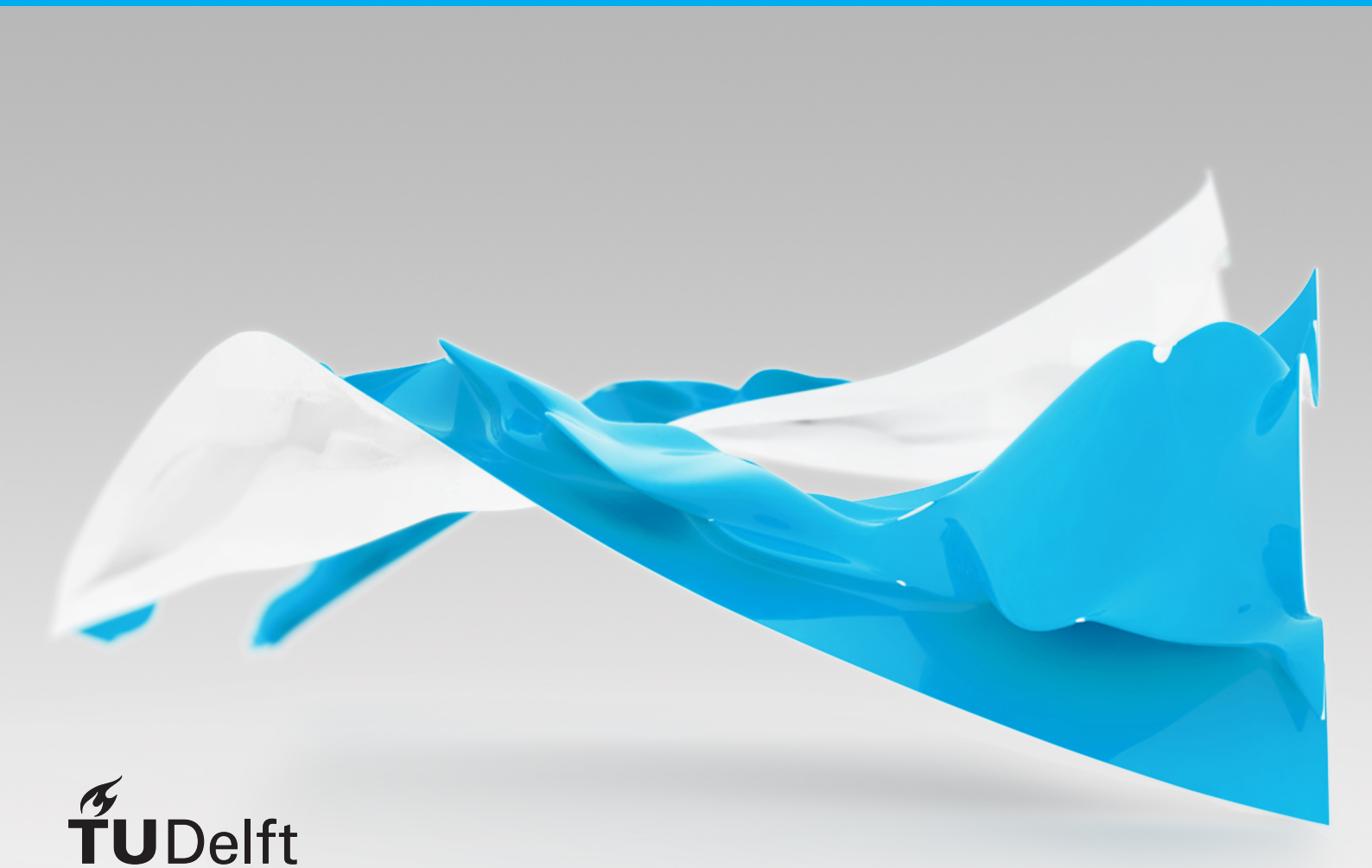

TU Delft

A Characterization Method for Hard-Soft Material Interfaces in Structural Optimization

by

Paul van Houten

to obtain the degree of Master of Science
at the Delft University of Technology,
to be defended publicly on Friday December 3, 2021 at 10:00 AM.

Student number:	4356500	
Project duration:	March 2, 2020 – December 3, 2021	
Thesis committee:	Prof. dr. A. A. Zadpoor,	TU Delft, supervisor
	Dr. M. J. Mirzaali,	TU Delft, supervisor
	Dr. P. Dey,	TU Delft
	Ir. M. Cruz Saldivar,	TU Delft

An electronic version of this thesis is available at http://repository.tudelft.nl/.

TU Delft

Preface

"Nature is our biggest ally
and our greatest inspiration.

We just have to do
what nature has always done.

It work out the secret of life long ago."

-Sir David Attenborough (2020)

It is with joy that I present this thesis that concludes my Master's education in Mechanical Engineering. This work represents the topics that motivate and inspire me the most. Over the last several years of my time at the TU Delft, I have started to admire material sciences, learn the principles of engineering optimization, and grasp on the fundamentals of additive manufacturing. During my internship at Toyota, my desires to apply my knowledge on technological innovation were expanded. The challenges encountered in the automotive industry showed surprising amounts of overlap with the research interests at the TU Delft department of BioMechanical Engineering. However, what started with a graduation collaboration with Toyota in Belgium, ended in doing research at the TU Delft. Here, I was fortunate enough to get the opportunity to make that common challenge become the foundation of this thesis.

First and foremost, I need to stress that finalizing this thesis would not have been possible without the great support from everyone involved. I take this opportunity to thank and express my appreciation to my professor Amir Zadpoor who has introduced my thesis proposal to the Biomaterials & Tissue Biomechanics research group.

To my supervisor Mohammad Mirzaali who has been a key figure in keeping me on track. Thank you for taking the time to keep up with my progress along the way. I consider our meetings valuable from which I greatly appreciate the encouraging and solution-oriented feedback.

To Mauricio Cruz Saldivar who enabled me to make this thesis to be more than I could have imagined. Thank you for sharing countless hours in 3D printing, painting, testing, reading and drinking coffees. You single-handedly taught me everything I needed to know to present this thesis as is. I enjoyed and am very grateful for every single minute of your support.

To my friends and my girlfriend who I have probably exhausted with my ongoing monologues about this thesis. Thank you for listening and providing me with the motivational responses that changed my perspective.

Ultimately, I would like to share my deepest gratitude to my parents who have given me the opportunity to develop myself to where I am today. Thank you for you endless support, interest, and motivational faith in me.

Paul van Houten
Delft, December 2021

Abstract

The distribution of multiple materials within a single structure is a strategy that various biological systems rely on to achieve outstanding mechanical performances. These biological examples illustrate the effective utilization of hard rigid and soft flexible materials in particular. The proper composition of such hard-soft materials exceeds the structural limitations found in their individual material counterparts. The manufacturing of hard-soft material structures is especially relevant today due to recent developments in additive manufacturing that certify the technology with local material-specific functionalities and enlarged design spaces. However, to unravel the next generation of unprecedented structural performance, today's state of engineering and research has yet to overcome the challenges encountered in multi-material design. The dissimilar material junctions within multi-material structures are prone to load transmissions, so they carry a crucial structural responsibility. Therefore, the interface design process must be subjected to representative interface characteristics which are often overlooked in the literature. In this work, we present a method to characterize and model multi-material structures to provide an optimal interface design in terms of the multi-material's joining strength.

We consider the joining strength of 3D printed hard Verocyan and soft Agilus30 by its fundamental joining principles of material bonding and mechanical interlocking. Material bonding is characterized by the extent of allowable traction between the two materials. We experimentally quantify the loading-dependent critical stress at which interface debonding initiates through mapping of digital image correlation deformations on a finite element model. We numerically define the extent of mechanical interlocking by the force required to achieve an unlocked multi-material state. The finite element models contain experimentally calibrated elastoplastic and hyperelastic material models to represent the hard and soft material behaviors, respectively. Subsequently, a structural optimization based on a genetic algorithm iteratively updates a constrained parametrized interface design according to material bonding and mechanical interlocking objectives.

The numerical evaluations of calibrated hard and soft material characteristics show good agreement in structural response with their real-world equivalents. The digital image correlation deformation method successfully acquires the loading-dependent critical stresses at which the two materials debond from one another. The finite element analyses of individual joining principles adequately determine a design's material bonding and mechanical interlocking performances. The optimization's objective function value evolution suggests a trade-off in joining contributions where mechanical interlocking maximizes performance in more shallow, wider interface designs, whereas material bonding performs better in narrow, deeper ones. Validation experiments illustrate the dominating contribution of material bonding in A30-VC structures. Optimizing for two distinct hypotheses of interface failure equations shows no significant difference in physical joining strength. However, they do support the concept that the interface characteristics affect the optimal joining shape. Despite adequate estimation of the individual joining principle performances, a more accurate approximation of the multi-material physical joining strength necessitates the consideration of the effects induced by the interaction of material bonding and mechanical interlocking. Nonetheless, this work underlines the emphasis regarding interface characteristics in the promising structures of multi-material.

Contents

List of Figures

Nomenclature

Abbreviations

$A30$	Agilus30
AM	Additive Manufacturing
$ASTM$	American Society for Testing and Materials
CZM	Cohesive Zone Model
DIC	Digital Image Correlation
FEA	Finite Element Analysis
FEM	Finite Element Method
GA	Genetic Algorithm
$LEFM$	Linear Elastic Fracture Mechanics
$NLPQL$	Non-Linear Programming by Quadratic Lagrangian
SO	Structural Optimization
TO	Topology Optimization
VC	VeroCyan

Symbols

α	Power-law exponent
$\bar{I}_1$ and $\bar{I}_2$	left Caucy-Green deformation tensor invariants
ϵ_p	Plastic strain
ϵ_t	Total strain
ϵ_{eng}	Engineering strain
ϵ_{vm}	Equivalent Von-Mises strain
$\mathbf{C}$	Interface curve directional vector
$\mathbf{L}$	Loading directional vector
$\mathbf{x}$	Mooney-Rivlin set of design variables
ϕ	Local loading direction
$\boldsymbol{\chi}$	Interface optimization set of design variables
σ	Material stress
$\sigma_{45,c}$	45 degrees critical interface stress
$\sigma_{\perp,c}$	Mode I critical interface stress
$\sigma_{\parallel,c}$	Mode II critical interface stress
$\sigma_{A30,c}$	Critical Agilus30 strength
σ_{A30}	Agilus30 strength
σ_{db}	Critical debonding stress of the interface
σ_{eng}	Engineering stress
$\sigma_{M,c}$	Mixed-mode critical interface stress
σ_{VC}	VeroCyan strength
σ_{vm}	Equivalent Von-Mises stress
A_{14}	Design's volume ratio constraint
c_{01}, c_{02}, c_{10}, c_{11} and c_{20}	Mooney Rivlin material constsants
C_{end}	Sample cross-section at the end of loading
C_{Start}	Sample cross-section at the start of loading
d	Mooney-Rivlin incompressibility parameter
E	Material stiffness
E_{A30}	Agilus30 Young's Modulus
E_{VC}	VeroCyan Young's Modulus
f_T	Interface optimization mean objective function value
$F_{exp,i}$	Measured force at displacement step i
$F_{FEA,i}$	Calculated force at displacement step i
$f_{MB}(\boldsymbol{\chi})$	Interface optimization material bonding objective function

$f_{MI}(\boldsymbol{\chi})$ Interface optimization mechanical interlocking objective function
$f_{MR}(\mathbf{x})$ Mooney-Rivlin optimization objective function
G_I Crack energy release rate
J Deformation gradient determinant
K_I Stress intensity factor
L_i Node-to-node length of the interface
L_{tot} Total length of the interface
$m_{\perp}$ Proportion of loading normal to the interface
$m_{\parallel}$ Proportion of loading tangential to the interface
n Number of nodes on the interface
$P_1 - P_4$ Positions of the four interface curve control points
R^2_{ϵ} Interface strain correlation of determination
R^2_{σ} Interface stress correlation of determination
R^2_{A30} Agilus30 correlation of determination
R^2_{MB} Material bonding correlation of determination
R^2_{VC} VeroCyan correlation of determination
s Distance along the interface
u Displacement
v Integer number of periodic repetitions of interface designs
W Mooney-Rivlin strain-energy potential
w Interface design's width
x_c and y_c x- and y-vector components for the nodal curve direction
x_l and y_l x- and y-vector components for the nodal loading direction

1 Introduction

1.1. Motivation

Multi-material structures have the fascinating capability of outperforming their individual materials' mechanical performance. The proper distribution of dissimilar materials allows for, among others, locally varying structural responses, reduced material usage, and increased fracture resistance. Many of these advantages are considered simply infeasible with monolithic structures. The composition of multiple materials within the same structure carries the potential to, perhaps counterintuitively, exceed the capabilities of the less performing mono-materials. Therefore, proper engineering of multi-material structures surpasses traditional engineering where the monolithic structure's limitations are found when no more material can be removed without the structure failing under certain loading conditions. Such benefits are beneficial for lightweight structure applications, like those encountered in the aerospace, automotive, and biomedical industries. Especially hard-soft material structures show to provide improved mechanical performance [1], similar to the hard-soft segments in the molecular architectures that make the prominent polyurethane plastics so favorable for many applications [2]–[4]. From a molecular standpoint, polyurethanes mimic the architectural structures of natural spider silk and nacre, known for their outstanding strength and toughness [5], [6]. For these excellent combined mechanical properties of hard and soft segments, polyurethane plastic materials are one of the most versatile and renowned materials in the majority of today's biomedical applications and engineered products [7], [8].

Numerous traditional methods are readily available for the manufacturing of multi-material structures. Joining technologies such as derivatives of molding and thermal joining processes enable the manufacturing of multi-material structures through adhesive bonding, mechanical interlocking, or a combination of these mechanisms [9]. Consistently, these methods rely on additional processes for the joining of multiple materials. Moreover, due to technological constraints, these methods produce structures with little geometric complexities over a limited range of materials. On the other hand, additive manufacturing (AM) technologies are known for their capability of building geometrically complex parts, generally in a single step [10]. Recent developments in AM have led to the support of multi-material AM, certifying the technology with material-specific functionalities and subsequently enlarged design spaces [11], [12]. This study will focus on the fabrication of multi-material parts with the use of voxel-based 3D printing. Voxel-based 3D printing is a material jetting AM technology that is also often referred to as PolyJet 3D printing. In essence, the technology shows great resemblance with traditional household 2D inkjet printers. Instead, a locally jetted photo-polymer material in the shape of small droplets is cured by exposure to UV light. The droplets, representing the 3D equivalent of a 2D pixel, *i.e.*, a voxel, obtain their final material characteristics once cured. Consecutive layers are jetted as the build tray moves downward, providing a final layer-by-layer manufactured part. A variety of supported materials facilitates the fabrication of varying material characteristics in a single part. These characteristics range from rigid to flexible for model materials and water-soluble for support materials [13]. En masse, multi-material AM promises unprecedented freedom of design by manufacturing tremendous geometric complexities with extended, locally varying material properties [14]. Such freedom of design enables highly personalized and efficient manufacturing motivating the production from

tailor-made patient implants to one-of-a-kind vehicle seating [14].

However, the challenge that arises with multi-material structures is the achievement of qualitatively profound interfaces among the individual materials [15]. An illustrative example is the sheer complexity of the interfaces found in bone-tendon connections. While bones are much stiffer to accommodate for multiple loading conditions, tendons have increased toughness to sustain significant tensile loads while also behaving in a compliant manner to allow for joint positioning. A sudden transition of dissimilar material properties, like those found in, but not limited to, bone-tendon interfaces can introduce high-stress concentrations [16], [17]. The dissimilar material junctions within multi-material structures are prone to load transmissions, so they carry a crucial structural responsibility. It is, therefore, not surprising that interface failure is commonly encountered in the shape of rotator cuff tear or the anterior cruciate ligament rupture. In addition, a dissimilar material interface undermines bonding performance due to the mixing of material properties in voxel-based 3D printing [18] and contact failure occurs at a lower stress than the strength of either material [15]. Therefore, emphasis must be put on the interface design process of multi-material parts taking into account the interface conditions. Several biological and engineering strategies currently attempt to tackle these interface challenges, as we will describe in section 1.3 and 1.4. First, we will briefly discuss the essential background information that is the foundation of many of those strategies.

1.2. Background

This section supports the general understanding of topics that lay at the foundation of the methods used in this work. We will briefly discuss the topic of Finite Element Analysis (FEA) as a structural analysis tool, followed by the relevant topic of cohesive fracture mechanics to represent multi-material interfaces. Subsequently, we will touch on the topic of Structural Optimization (SO) as a design tool. These tools are integrated with the engineering simulation and 3D design software Ansys. Therefore, in this work, we used Ansys® Academic Teaching Mechanical and CFD, Release 19.2 as our main tool for characterization, evaluation, and optimization.

1.2.1. Finite element analysis

FEA is the simulation of a, often structural, phenomenon based on the numerical technique of the Finite Element Method (FEM). The method approaches engineering problems by subdividing the total complex system into smaller problems or ‘elements’. As the behavior of these individual and much simpler elements is readily understood, one could study the original system by rebuilding it from these elements. Dealing with structural analyses, the assembly of calculated force-displacement relationships for each element allows for an approximation of complex structures’ structural responses. Naturally, the extent to which the original structure is subdivided or ‘discretized’ into a finite amount of elements determines the accuracy of the approximation as well as the computational expense to obtain it. The process of approximating the behavior of a continuum under the FEM is generally considered a task well designed for digital computers, even when the amount of elements becomes substantial [19]. The FEM is a widely adopted method for problems encountered in heat transfer, fluid flow, electromagnetics, and structural analysis. In this work, the FEA is an essential component in performing structural analyses on different multi-material geometries with varying fracture mechanics. As such, we will introduce the relevant fracture mechanics now.

1.2.2. Fracture mechanics

Fracture studies commonly rely on the theory of linear elastic fracture mechanics (LEFM) to solve fracture problems. The conditions for LEFM to be valid require the existence of a sharp initial crack where the concentrated stresses near the tip of the crack create a so-called process zone [20]. A further requirement is that the size of the process zone remains relatively small with respect to the fracture sample. Once the conditions for LEFM are satisfied, one can characterize a crack by local parameters such as the stress intensity factor, K_I, or energy release rates, G_I. However, for cracks along a multi-material interface, K_I either approaches zero or infinity as a result of the elastically mismatched interface [21]. Therefore, as an alternative approach to that of LEFM, the cohesive zone model (CZM) was proposed. The CZM overcomes many of the above drawbacks encountered in LEFM and has shown

successful applicability in many interface related fracture problems, including multi-material design [22], [23]. In addition, it is widely accepted for its ease of implementation in FEM [24]. A traction-separation law lays at the foundation of a range of CZM implementations. The traction-separation law relates, as the name implies, the traction and separation of the interface. With increasing separation, the traction first increases to maximum stress, after which it diminishes to allow for complete debonding (Figure 1.1) [25], [26]. This approach can be extended to account for mixed-mode loading conditions, ranging between normal and tangential loading directions for the interface. Therefore, the physical interpretation of the CZM describes the fracture of the interface by characterizing the initiation and propagation of debonding.

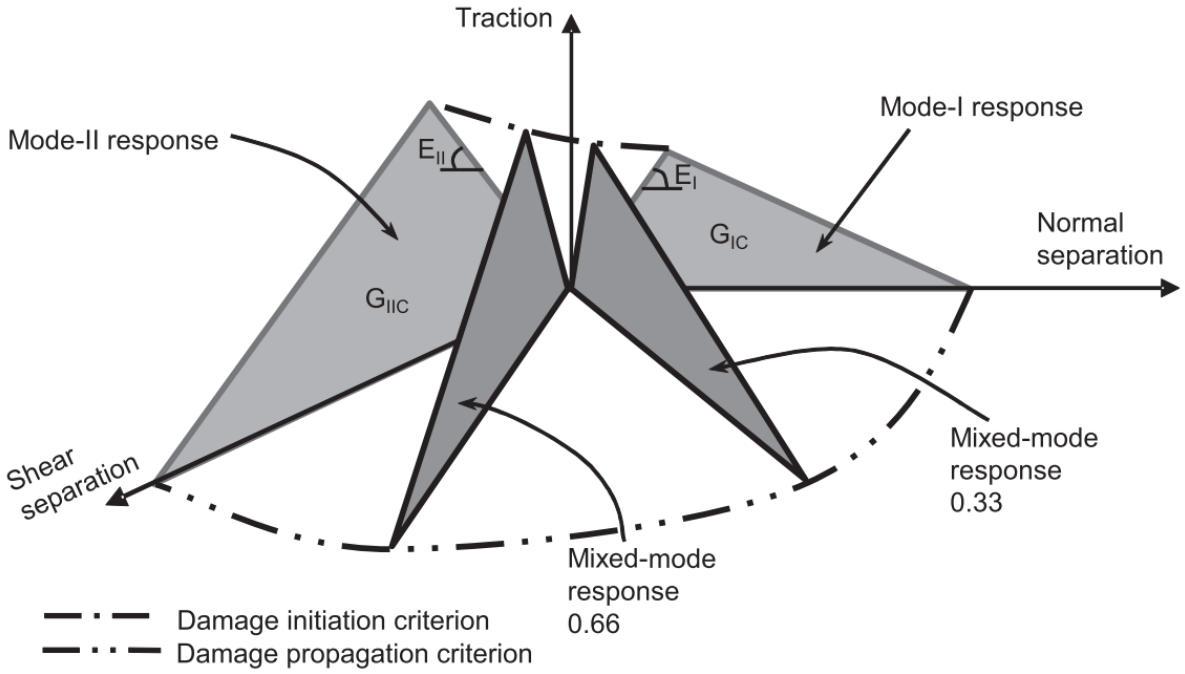

Figure 1.1: Bilinear example of a loading-dependent traction-separation law, commonly used cohesive zone models (CZM). Taken from [26].

1.2.3. Structural optimization

Structural optimization (SO) describes the process of distributing material within a design domain so that it improves a user-defined objective subject to constraints imposed by a variety of disciplines. This process achieves an optimal structural result when no further improvements are feasible. Within SO, we differentiate between the three types of size, shape, and topology optimization (TO) (Figure 1.2) [27]–[29]. In size optimization (Figure 1.2a), the structural domain is known and fixed throughout the process, where the size of geometric features is variable. In shape optimization (Figure 1.2b), the structural domain is known, but not fixed, therefore also considers the internal and external boundaries as a variable. Lastly, topology optimization (Figure 1.2c) allows for the most significant design alterations within SO as its design variables also enable the introduction and removal of topological features in the form of cavities in the design domain. The general SO problem formulation consists of an objective function, design variables, and constraints. Combined with an iterative updating algorithm, they enable the search for an optimal structural design. In this work, we focus on the algorithm class of genetic algorithms (GA). These algorithms function by generating numerous designs simultaneously and systematically searching for improved objective functioning designs by interactions between each generation of designs. GA are advantageous to other algorithms in the regard that they do not require dedicated sensitivity analyses [28]. Furthermore, due to a more random search method, one can acknowledge the favorable robustness in GA [30]. For these reasons, GA are applicable for the SO of multi-material designs that consider interface conditions [31]. En masse, the SO commonly utilizes a FEM to obtain relevant structural responses. Significant to multi-material interface design, these struc-

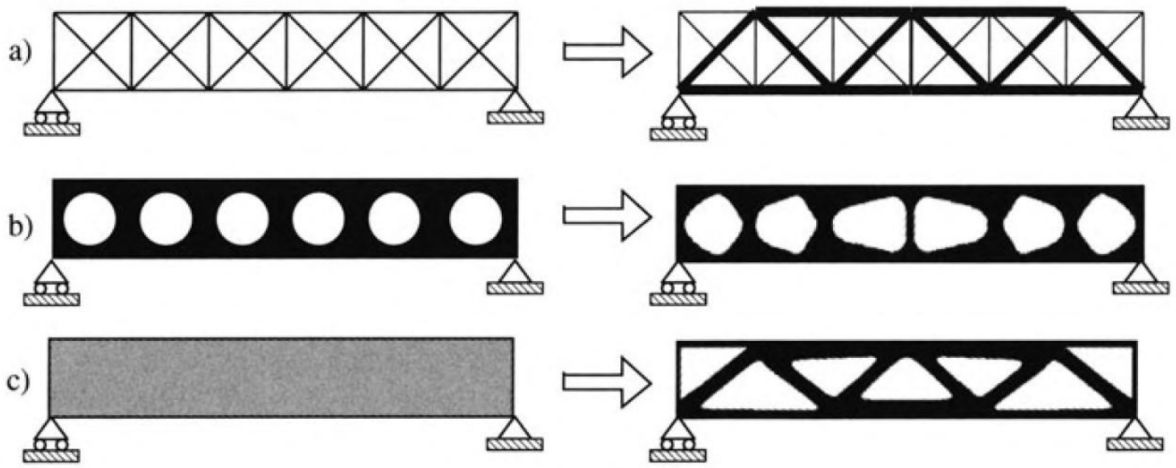

Figure 1.2: Three categories of structural optimization (SO), before (left) and after (right) optimization alterations. (a) Size optimization, (b) shape optimization, and (c) topology optimization. Taken from [29]

tural responses could reflect upon the fracture mechanics involved.

1.3. Biological strategies

The use of multi-material structures is not uncommon and certainly not invented recently. Numerous biological strategies make use of multiple materials for strengthening or fracture resistance purposes. Their current material topologies are a result of millions of years of evolution. We briefly examine two biological functions that are related to material interfaces. First, the function of permanently attaching governs how bonding can withstand forces that would otherwise result in undesirable debonding. Secondly, we observe the function of preventing fracture. In this class, the results describe how mechanisms function as a crack deflection method to prevent fracture.

1.3.1. Assembly of a permanent bond

The Venus' flower basket is a glass sponge animal at the bottom of deep waters [32]. They process food and oxygen from the water while maintaining their position on the ocean floor. They achieve this by anchoring themselves in the sediment with thousands of long hair-like skeletal elements called spicules. These spicules are geometrically characterized by having backward-facing barbs along their length and with a crown-like shape at the end (Figure 1.3.A-B). A multiplicity of these spicules ensure a sufficiently strong bond. Similar to the sponges' spicules, the Greta oto caterpillars also make use of backward-facing barbs to achieve a robust bonding interface (Figure 1.3.C-D) [33]. The caterpillar does so to undergo complete metamorphosis into a butterfly safely. The backward-facing barbs, or hooks, are arranged over a curved surface inserted into an earlier fabricated pad of silk fibers. The silk fiber pad consists of many tiny loops that, by also considering the hooks' interlocking, closely resemble the working principle of Velcro. The established interface, primarily relying on mechanical interlocking, provides the necessary support to protect it from stresses caused by, for example, strong winds. Furthermore, the roots of English ivy achieve yet another interface design [34]. It succeeds in attaching to nearly any surface using a multi-stage strategy. First, the thin roots under the stems emit a natural sticking substance for initial adherence to a surface, followed by a shape change of the roots that have grown into a surface cavity for anchoring (Figure 1.3.E-G). One can observe that the former mechanism relies on an adhesive material bonding whereas the latter mechanism, again, relies on mechanical interlocking. The loss of water within the roots, *i.e.*, drying, establishes their shape change which enables its anchoring capabilities. These capabilities benefit from highly structured substrate surface cavities as they provide greater degrees of interaction. From the above biological strategies for achieving a permanent bond, one can observe that all considered designs make use of a large number of relatively weak attachments that, when combined, form a sufficiently strong bond. Moreover, mechanical interlocking resembles the dominant mechanism in achieving these multi-material connections. However,

in the occasion where there is lack of mechanical interlocking capabilities, adhesive bonding becomes essential in achieving a firm connection.

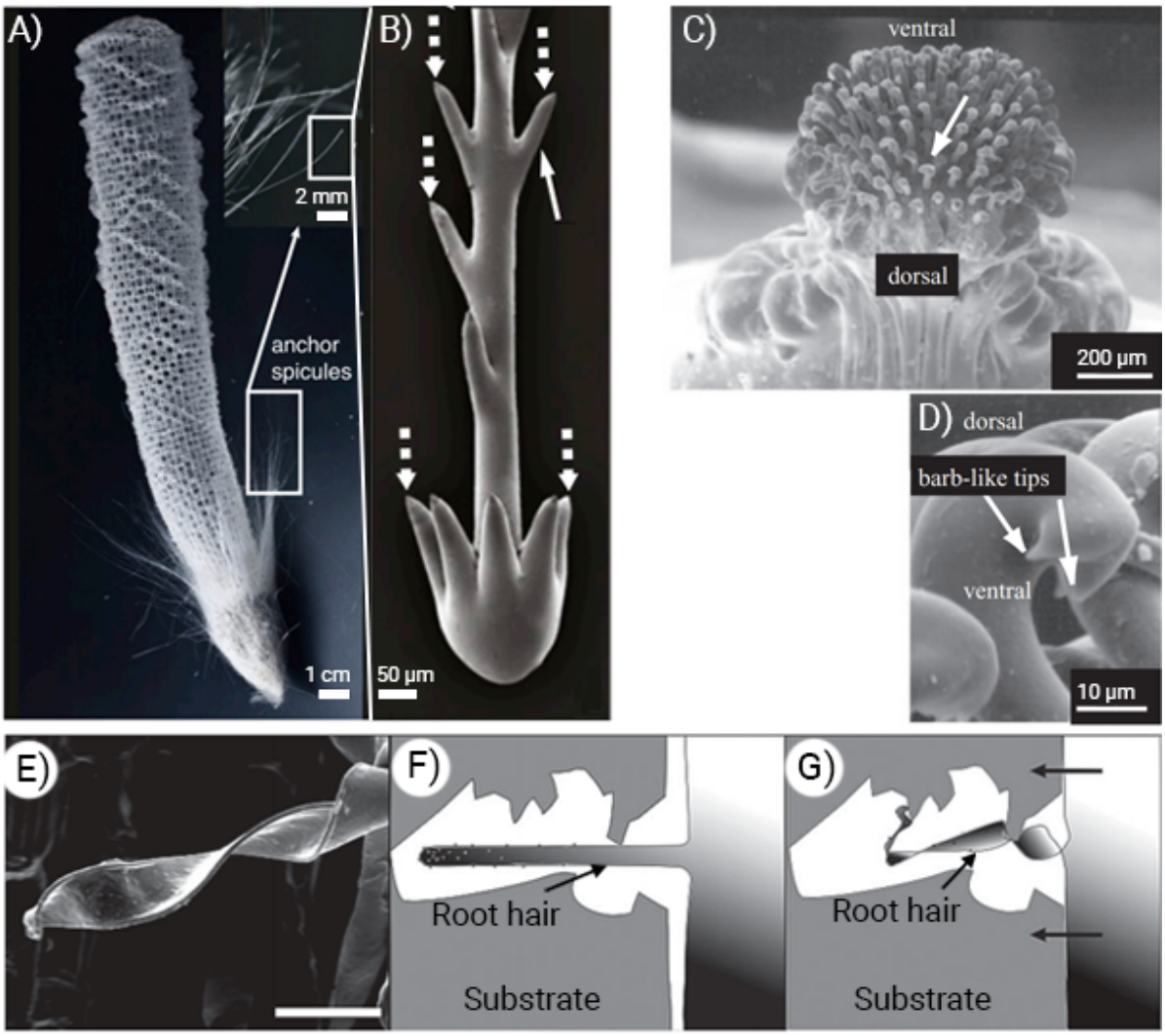

Figure 1.3: Biological strategies of achieving a permanent attachment. (A) The Venus' flower basket glass sponge animal with its backward-facing barbs and a crown-like shape along its spicules (B) [32]. (C) The rear end of a Greta Oto caterpillar consists of backward-facing barbs (D) [33]. (E) A single English ivy root, interlocking before (F) and after (G) drying [34].

1.3.2. Prevent fracture

Several biological strategies function as mechanisms that prevent crack propagation, which appear particularly interesting as multiple materials fabricate them. One of these is the specific composition of nacre [6]. Nacre consists of mostly stiff and hard minerals. The interface mechanics that are distributed among the minerals control the nacre's structural behavior. As a result of the addition of soft organic layers, these interfaces arrange themselves similarly to a mortar in a brick wall (Figure 1.4.A). Such an arrangement is a toughening mechanism that deflects cracks via the interfaces, circumventing the crack propagation in the brittle parts. This particular arrangement of dissimilar materials achieves extreme overall structural toughness. Another biological strategy is that of the wing structure of the desert locust Schistocerca Gregaria (Figure 1.4.B-C) [35]. Its structure revolves around a similar biological strategy that handles the presence of cracks rather than preventing them from inevitably occurring. Its wings consist of a lattice structure of veins that supports a thin fragile membrane. The distribution of these veins is optimally scaled such that it defines membrane patches that match the critical crack length of the membrane material. Acting as a barrier to crack propagation, the veins prevent cracks from exceeding their critical length for self-propagation. Therefore, cracks that are present in the membrane

are not able to reach a critical length. Consequently, cracks will not propagate through the remainder of the wing. Membrane patches that are larger than this critical crack length would allow for initial cracks to propagate. In contrast, membrane patches tinier than the critical crack length would be an inefficient use of vein material. The currently evolved state of the wing is exemplary in a lightweight design with high resistance against crack propagation, *i.e.*, fracture toughness. Finally, perhaps one of the most complex and also the most crack-resistant substances found in nature are those of horse hooves (Figure 1.4.D-E) [36]. Localized loads often subject horse hooves to tremendous amounts that could fatefully harm the animal. Although composed of similar materials known to humans as nails, its morphology includes hollow tubes defined by stacked rounded planes of similar material. Its purpose is a crack diversion mechanism that prevents cracks from propagating and redirecting them in less harmful directions. Cracks that initiate in, for example, an upward orientation are redirected towards the outer hoof surface, away from the foot's living tissues. The above biological strategies for preventing fracture illustrate that the introduction of often softer materials carries the potential to increase fracture toughness. Furthermore, a particular material morphology introducing similar material discontinuities enables the deflection of cracks successfully. Note that these mechanisms assume the inevitable presence of cracks and, therefore, focus on minimizing fatal crack propagation instead of crack initiation.

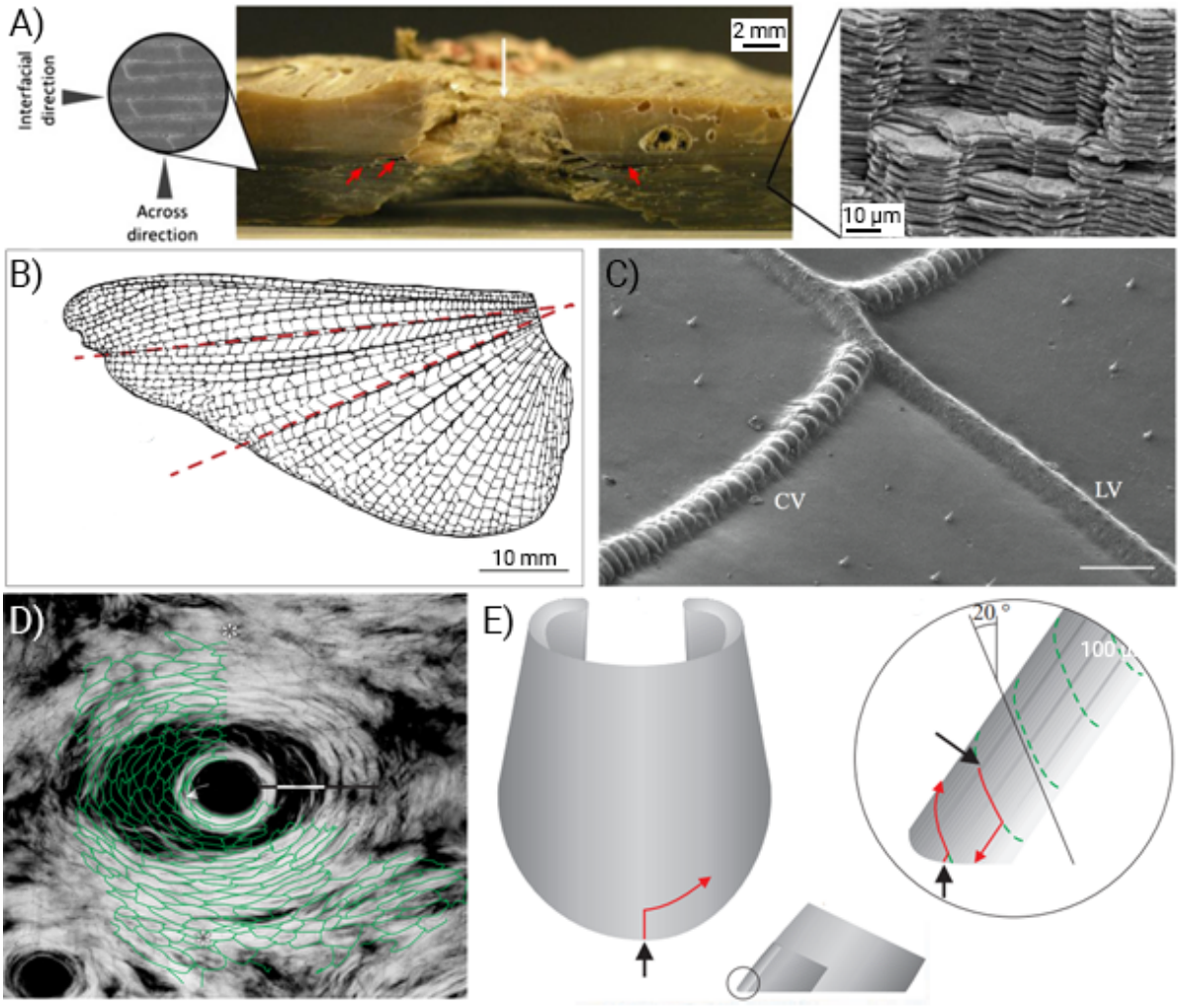

Figure 1.4: Biological strategies that prevent fracture. (A) The brick-and-mortar-like structure of hard minerals and soft organic layers found in nacre [6]. (B) The wing structure of the desert locust Schistocerca Gregaria with crack-obstructing veins (C) distributed through the fragile membrane [35]. (D) Hollow tubes inside the horses' hoove wall that redirect incoming cracks (E, black arrows) to less harmful directions (E, red arrows) [36].

1.4. Engineering strategies

Many industries could benefit when one would successfully achieve the optimal design of an interface in multi-material structures, perhaps similar to those found in biological strategies. Driven by the increasing need for economic and ecologic sustainability, many industries and research areas are challenged with innovative, high-performance products. Multi-material components might offer a solution to keep up with the most recent global environmental legislation for emissions while reducing costs introduced by energy and raw materials. Current literature reveals numerous works dedicated to diverging industries that involve the interface challenge.

In dentistry, Couegnat et al. [37] and Shi et al. [38] examined the design optimization of cavity shapes for restoration purposes. Both studies investigated the tooth-restoration interface. Their objectives defined the minimization of localized interfacial stresses to prevent crack-initiated fracture. As a result of simulating several bonding conditions, the interface conditions were found to significantly impact the structure's stress distribution [37]. By investigating two contact extremes of perfectly bonded (no sliding or separation allowed) versus debonded interfaces, reduced interfacial stresses were found due to the interface shape adaptation [38]. These studies then illustrate that one can approach the interface from two aspects, considering interface characteristics and its shape. In the former aspect, the interface conditions affect the adjacent structure's stress distributions. Therefore, one must be aware of the essential contribution of interface characteristics in multi-material design. While in the latter aspect, the interface shape affects the interfacial stresses as a result of varying loading directions. Thus, structural optimization of the interface design that includes the anisotropy of principal loading enables one to alter how the interface is stressed.

Within Biomechanical engineering, Moussa et al. [39] considered cementless porous acetabular reinforcement implant design. Their objective was to minimize the elastic modulus mismatch that would otherwise result in undesirable micromotions. However, the contact conditions were defined as frictionless and therefore merely take into account the effect of mechanical interlocking. In contrast to a frictionless contact definition, it is a common practice to assume perfectly bonded interfaces in the modeling of tendon-to-bone attachments [17] and other bio-inspired adhesion of micropatterned surfaces [40]. Again, underlining the focus on the multi-materials structure's sensitivity towards the shape of the interface and not the interface conditions themselves. As these decisions for frictionless or perfectly bonded interfaces often lack the support of argumentation in literature, we assume the use of these interface conditions are a matter of simplification in numerical modeling. Notwithstanding, we notice that the effect of such assumptions is often overlooked or overshadowed by the insights obtained on the mechanical interlocking aspect of the interface.

An example of not properly considering the interface conditions is further illustrated by the work of Klarbring et al. [41] in which the authors considered the optimal design of adhesively bonded patches for structural repair in aerospace applications. Modeled adhesive layers represent the bonding of the repair patch to the cracked specimen. However, the adhesion strength is not discussed, nor is the effect of the adhesion strength investigated. The lack of considering the adhesion strength leads to the point where a failure of the bonding is not defined. Essentially simulating a perfect bond as no sliding or separation could initiate. Despite the objective being to optimize the crack energy release rate through the shape of the repair patch, the characteristics of the interface, *i.e.*, the adhesive layer, could very well contribute to obtaining this objective. For that reason, not only is material bonding required to be modeled in optimization problems, so are the requirements in derivating accurate interface characteristics.

Similar to the aerospace industry, the automotive industry also requires progressive reductions in weight. Li et al. [42] developed a multi-material topology optimization algorithm to achieve lightweight designs for automotive applications. A material extrapolation function determines the morphology of the two available materials within the design domain. Two dissimilar materials arranged next to each other result in an interface amid the materials. Despite the author's recognition of interface conditions in multi-material topology optimization, they did not bother to define any in their FEM. Consequently, the interface consideration was perfectly bonded. It again emphasized the common simplification of interface characteristics without any support for argumentation or discussion on such assumptions.

Fortunately, a small amount of researchers is aware of commonly simplified modeling of interfaces in multi-material structural optimization [22], [23], [43]–[45]. Liu et al [22] investigated problems that include the failure of a bonding interface compared to perfectly bonded interfaces. The authors achieved the failure of a bonding interface through an exponential CZM. As a result, the interface characteristics strongly affected the optimal design and therefore the multi-material morphology differed fundamentally from its perfectly bonded counterpart. However, the chosen interface parameter values, such as the fracture energy, maximum traction, and separation of the interface, are replicated from Hilchenbach et al. [43], which does not support any argumentation of these values. Although several interface parameter values were explored, the characteristics that represent real-world interfaces remain unclear. Another noteworthy aspect of the work of Liu et al. [22] is that their optimal multi-material morphology lacks interlocking mechanisms over the interfaces, unlike those found in [23]. A parametric design incapable of generating geometric detail could prevent the formation of such mechanical interlocking mechanisms. At this point, it should be noted that the challenge of generating multi-material structures is two-fold. This is explained by the contributions to the joining strength of the entire interface structure. The joining strength is affected by the adhesive bond between the dissimilar materials and the extent of mechanical interlocking [46]. To obtain the optimal interface design, a model must bear the capacity of simulating both aspects that affect the joining strength.

By now, one may break down the joining strength of multi-material interfaces by their contributions to interfacial stresses. The two-fold contribution in multi-material joining strength relates to the aspects that affect the interface stresses mentioned earlier in this section, namely the interface characteristics and shape. In other words, the interface characteristics and shape aspects that determine interfacial stresses represent the material bonding and mechanical interlocking that determine the multi-material joining strength, respectively. Despite the compatibility of the combined contributions of material bonding and mechanical interlocking in FEM and SO, minimal research dedicates the combined description to multi-material design. Considering today's advanced state of numerical modeling, fracture mechanics and SO, we are triggered by the further investigation of multi-material design that carries great potential in various industries and research.

1.5. Research definition

In this work, we propose a method to model multi-material structures including the interface characteristics. The goal is to provide an optimal design in terms of the multi-material's joining strength. The optimal design, therefore, takes into account a numerical approach to conclude on the material bonding and mechanical interlocking aspects. The model intends to be used for hard-soft material interfaces and therefore supports hyperelastic and elastoplastic material models simultaneously. Experimental simulations allow for the calibration and validation of the numerical simulations. We demonstrate the purpose of the model via a structural optimization of the interface design. In contrast to traditional stiffness optimization, we consider a user-defined objective function that regards both aspects of the joining strength. The optimization results provide insight into how dissimilar material bonding and mechanical interlocking cooperate to achieve the final joining strength.

Raised by our interest in material bonding, we ask how dissimilar material bonding can be modeled, based on realistic interface characteristics. We hypothesize that the dissimilar material bonding can be modeled based on the principles found in applying a CZM for contact. This modeling would imply the use of interface characteristics representing the material bonding strength in terms of traction. We expect to obtain such interface characteristics from local measurements on experimental multi-material samples. The lack of experimental standards for testing hard-soft material interfaces under multiple loading conditions might indicate the challenges in acquiring accurate interface characteristics.

Following our interest in mechanical interlocking, we ask how mechanical interlocking can be modeled based on realistic material characteristics. Here, we hypothesize that extent of mechanical interlocking is determined by the amount of loading required to reach an 'unlocked' state. For hard-soft material interfaces, this reduces to accurate modeling of the diverse intrinsic material characteristics of

rigid and flexible materials. Here, we expect a hyperelastic material model to capture the soft material's behavior. In contrast, a multi-linear isotropic hardening material model will capture the elastoplastic behavior of the hard material. The error between experimental and numerical simulations is a measure of the accuracy of the material models. We expect to minimize this error through optimization algorithms. The optimization actively modifies the material model parameters such that the numerical results best fit the experimental results. We take the mechanical interlocking aspect of joining strength to be accounted for in optimization through a dedicated objective function.

Subsequently, we ask how one can optimize a dissimilar material interface design for optimal joining strength. We expect that a structural optimization approach allows for achieving the optimal joining strength. In this approach, the multi-material structure will be modeled by a parametric design, defining individual material domains and, therefore, the interface's shape. An objective function constructed by the FEA on material bonding and mechanical interlocking performance determines the direction of optimality. Subsequently, a robust GA is expected to find the optimal solution most efficiently. Nonetheless, due to the size of the solution space and the computational expense of a single FEA, it is expected that the complete optimization will be time-consuming.

Finally, these subquestions lead to our primary interest and research question, asking how hard-soft material bonding and mechanical interlocking affect the multi-material structure's optimal joining strength. We hypothesize that both dissimilar material bonding and mechanical interlocking affect the structure's joining strength distinctively. Ultimately, we expect the bonding characteristics to affect the resulting optimal shape of the interface. Strong interface bonds in normal direction are expected to provide distinct optimal interface designs in contrast to interface bonds that have dominating strength in the tangential direction.

2

Methods

The primary method in this work is divided into two subjects, with either one having the purpose of elucidating the relevant research question. First, the methods for modeling the material and interface characteristics elaborate on why and how the specific characteristics are sought. The subsequent subject concerns the SO of the interface geometry.

2.1. Material & interface modeling

In this work we consider the interface characteristics to define the extent of adherence among the two materials. Although no adhesives will be used in this work's multi-material parts, it may be convenient to perceive the interface between dissimilar materials as a fictitious, zero-thickness adhesive. Distinct interface characteristics, such as greater maximum traction, would resemble a strong adhesive, whereas lower maximum traction would resemble a weaker adhesive. The CZM utilizes a similar approach of applying a fictitious, zero-thickness material in computational models with contact. Many applications of the CZM follow a bilinear traction-separation law [23], [47], [48]. Among the aforementioned maximum traction, further interface characteristics conclude on the interface's stiffness and critical fracture energy density (Figure 1.1). Although the latter characteristics allow for the numerical simulation of complete interface debonding including debonding propagation, we solely focus on the initiation of interface debonding as it will be sufficient to investigate the effect on the optimal interface design. We define the initiation of debonding at the point of maximum traction, *i.e.*, the critical stress. Therefore, concerning the CZM approach, we only consider its dimension of traction.

In the first part of this work, we describe a methodology to capture the interface characteristics in hard-soft material parts. Here, we take into account the direction in which the interface is loaded. Therefore, we investigate the magnitude of the maximum stress and its dependency on the loading direction. Similar to how the CZM operates in two-dimensional problems, we differentiate mode I (normal to the interface) from mode II (tangential to the interface) failure (Figure 1.1). We define any loading condition between these two extremes as mixed-mode loading. Capturing the interface characteristics from manufactured hard-soft material parts allows one to indicate whether the critical stress is loading-dependent on the specific material combination. Our method relies on the combination of mechanical testing and numerical modeling to find the, potentially loading-dependent, critical stress of the interface.

2.1.1. Characterization experiments

We utilize the technology of AM for obtaining multi-material parts. We used a commercial polyjet 3D printer by Stratasys of the model ObjectJ735 Connex3. The polyjet printer supports printing both hard and soft materials in a single print job. The materials considered in this work are Stratasys' VeroCyan (VC) and Agilus 30 (A30) for the hard and soft materials, respectively. VC is characterized by Young's Modulus of $E_{VC} = 2.2\ GPa$ and strength of $\sigma_{VC} = 50\ MPa$, whereas A30 has Young's Modulus of $E_{A30} \approx 1\ MPa$ and strength of $\sigma_{A30} = 1\ MPa$. These divergent material properties may support one's initial impression of how dissimilar the two considered materials are.

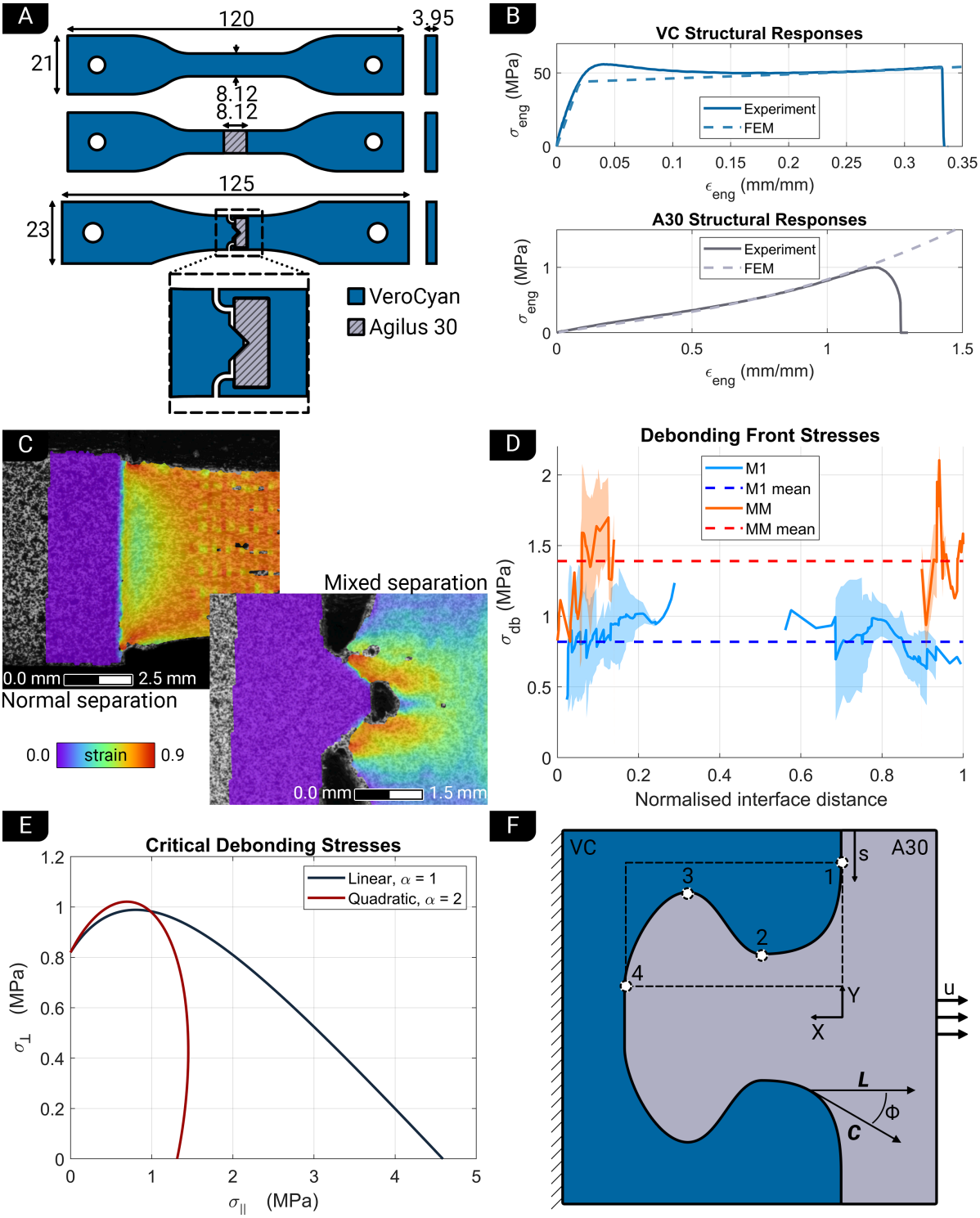

Figure 2.1: (A) From top to bottom: monolithic, mode I interface and mixed-mode interface characterization tensile samples. The samples have equal thickness and dimensions are in mm. (B) Structural responses for individual Agilus30 (A30) and VeroCyan (VC) materials. (C) Digital image correlation (DIC) deformation mesh colored overlay on mode I (left) and mixed-mode (right) tensile samples. (D) Obtained equivalent stresses at the debonding front, σ_{db}, along the hard-soft material interface for mode I (M1) and mixed-mode (MM) loading conditions. The mean values represent the loading-specific critical equivalent stress of the interface. (E) The descriptions of the full mixed-mode loading-dependent critical stress at which the interface debonds for linear and quadratic extrapolation of the loading-specific critical stresses. (F) The parameterized interface by control points 1-4 that separates the design domain in two material domains. **C** and **L** present a nodal interface curve and loading directional vector, respectively. The dashed lines set up the design's bounding box and s defines the direction of distance along the curve.

To get their material characteristics correctly simulated in the FEA, we require simple uniaxial tensile tests on the individual materials. The samples originate from ASTM standard D638 type IV specimen for polymers (Figure 2.1.A). The VC sample consists entirely of a single material, whereas the A30 sample partially consists of A30 with adjacent stiffer VC for gripping capabilities. Their structural response could then be obtained through a process of error minimization described in the subsequent subsection.

Uniaxial tensile testing of multi-material samples allows for the characterization of the interface between the two materials. Especially the debonding under specific modes is of interest. Testing for mixed-mode debonding is especially challenging with the combination of hard-soft materials, which is underlined by a lack of experimental standards. Therefore, we again make use of the A30 sample introduced above in addition to a secondary, mixed-mode loaded sample. The former sample considers the loading direction perpendicular to the interface resulting in mode I debonding. The latter sample considers an inclined interface with the loading direction angled to load the interface partially in mode I and partially in mode II, *i.e.*, promoting mixed-mode debonding.

The experimental setup of the interface sample tensile tests consists of the Lloyd Instruments LR5K tensile machine accompanied by a Limess Q-400 dual-camera digital image correlation (DIC) setup by Dantec Dynamics. The tensile machine loads the multi-material samples in a vertical direction, while the two cameras optically measure the sample's surface from an off-center position (Figure 2.2.A). Two LED panels provide sufficient sample lighting from the center between the cameras which are positioned roughly 0.5 m from the sample. Before testing a sample, a calibration process on a checkerboard tile at the sample's tensile position generates a calibration file for the current setup containing relevant data on the coordinate system and the position of the two cameras in it. Subsequently, a multi-material tensile sample is fixed in the tensile machine grippers. The front-facing side of the sample is prepared with a black-on-white speckle pattern using an air spray gun to enable pattern recognition on the sample's surface deformations. The imaging frequency is 1 Hz during the applied loads at a deformation rate of 2 mm/min. Dantec Dynamics' Istra4D 4.6.5 software manages image processing and deformation correlations to provide essential local displacement data over a specified area of interest during the tensile test, *i.e.*, the DIC deformation mesh. This mesh is set up with a facet size of 21 mm and a grid spacing of 7 mm in Istra4D's correlation setup.

2.1.2. FEA as a tool for material characterization

The FEA of multi-material parts requires thorough attention to the modeling of the individual materials and the contact between them. As the material characteristics of VC and A30 are vastly different, each material requires a dedicated material model. We model the VC material with a multilinear isotropic hardening model to capture its non-linear elastoplastic behavior. Multilinear isotropic hardening relies on uniaxial experimental tensile data. Once acquired the engineering stress-strain data of VC, converting it to the multilinear isotropic hardening definition is relatively effortless. First, we define the yield stress and, therefore, at which point the material starts to deform plastically. Plastic strain, ϵ_p, is defined as the total strain, ϵ_t, minus the elastic strain (2.1).

$$\epsilon_p = \epsilon_t - (\frac{\sigma}{E}) \tag{2.1}$$

With σ and E the stress and material stiffness, respectively. At this point, entering all plastic strain values and their corresponding stress values allows Ansys to interpret the hardening model based on the Von Mises yield criterion [47].

In contrast to relatively rigid VC material, the flexible A30 material experiences large elastic deformations when loaded. Material models that cover such material characteristics are hyperelasticity models. Hyperelastic material models are common practice for applications that involve flexible elastomers, synthetic polymers, and biological materials [49]–[51]. In this work, we model A30 with the (nearly-)incompressible isotropic Mooney-Rivlin material model. To accurately capture the non-linear elastic behavior, we utilize the five-term variant of the model as lower-term Mooney-Rivlin models are unable to capture the elastic behavior with minimal error. The strain-energy potential for the five-term

Mooney-Rivling is of the following form:

$$W = c_{10}(\bar{I}_1 - 3) + c_{01}(\bar{I}_2 - 3) + c_{20}(\bar{I}_1 - 3)^2 + c_{11}(\bar{I}_1 - 3)(\bar{I}_2 - 3) + c_{02}(\bar{I}_1 - 3)^2 + \frac{1}{d}(J - 3)^2 \quad (2.2)$$

Where c_{01}, c_{02}, c_{10}, c_{11} and c_{20} are material constants and d the material incompressibility parameter. $\bar{I}_1$ and $\bar{I}_2$ are invariants of the left Cauchy-Green deformation tensor and J equals the determinant of the deformation gradient (equals 1 for incompressible materials). The ideal model contains a combination of the material constants such that the resulting structural response is identical to that found in experimental tests. To find that single combination of material constants, we introduce a process of error minimization between the numerical results and its experimental counterpart. We set up the minimization based on non-linear programming by quadratic Lagrangian (NLPQL), a gradient-based optimization method that finds optimal results through iterative numerical searches. This includes the definition of design variables, an objective function, and constraints. The five material constants compose the set of design variables, $\mathbf{x}$. The objective function, $f_{MR}(\mathbf{x})$, equals the cumulative error in applied force between the numerical and experimental results at 30 displacement reference points. We define a constraint on the location of the smallest cross-section to be in the center of the soft material. This constraint prevents solutions that have expanding materials under loading from being validated. This error minimization process embodies simultaneous calibration and validation of the A30 material's elastic structural response by contrasting the numerical to the experimental results. Equation (2.3) represents the optimization problem formulation for finding the desired Mooney-Rivling material constants.

$$\begin{gathered} \min_{\mathbf{x}} f_{MR}(\mathbf{x}) = \sum_{i=1}^{30} |F_{exp,i} - F_{FEA,i}(\mathbf{x})| \\ s.t.\ C_{end} - C_{start} \leq 0 \\ (\mathbf{x}) = (c_{01}, c_{02}, c_{10}, c_{11}, c_{20}) \end{gathered} \quad (2.3)$$

With $F_{exp,i}$ and $F_{FEA,i}$ the measured and calculated forces at displacement steps i, respectively. Here, the displacement for a single timestep is equal in both structural responses, *i.e.*, $u(F_{exp,i}) = u(F_{FEA}, i)$ for all i. The cross-section constraint ensures that the soft material's center cross-section at the end of loading (C_{end}) is smaller than at the start of loading (C_{start}) to avert material solutions that expand under loading. In this work, we neglect A30's strain rate-dependent behavior recognized in additively manufactured polymers as it would drastically increase the complexity of material modeling [52], [53]. To reduce the effect of strain rate-dependent properties, we target a fixed order of magnitude in strain rate for all tensile tests. Calibrating the hyperelastic material constants to this strain rate ensures a satisfactory structural response for A30 within a single order of magnitude of strain rate. Moreover, a relatively low strain rate reduces the extent of elastic non-linearity [53] in benefit of the hyperelastic material model's capability to accurately simulate A30's structural response.

Despite having modeled the relevant individual material characteristics, we yet have to consider material and interface damage. In multi-material parts, we consider two types of failure attainable. Failure could occur in one of the individual materials or within the interface which we will henceforth refer to as damage and debonding, respectively. Damage in the individual materials is accounted for via the SO constraint, which we will elaborate on in subsection 2.2.3. We define the constraint values based on the critical equivalent strain magnitudes corresponding to the individual materials. As the hard material barely deforms in response to the applied loadings, its constraint is disabled in benefit of the optimization's efficiency. The debonding of the interface on the other hand is more sophisticated as it holds a loading-dependent criterion. Essentially, the criterion describes when the two materials in a bonded state are about to debond. Here, we make use of the A30's equivalent stress magnitude at the interface as an indicator of when debonding is about to occur. Moreover, the magnitude of this critical stress varies, depending on the angle between the loading and interface directional vectors, $\mathbf{L}$ and $\mathbf{C}$, respectively (Figure 2.1.F). In other words, the criterion monitors the direction of loading at the interface to determine its critical stress. We will now discuss the methods for acquiring the critical stresses at which the particular multi-material junction debonds.

2.1.3. DIC deformation mapping

The process of mapping data is where the mechanical testing and the numerical model come together to acquire the critical debonding stresses (Figure 2.1.C). A more detailed description is provided in Appendix A. We illustrate this procedure of DIC deformation mapping in four steps (Figure 1.4). First, we make optical measurements of the sample's area of interest during loading using the DIC setup. These measurements contain images of prepared, high contrast speckle patterns, which Istra4D subsequently utilizes to generate the DIC deformation mesh. Next, we convert the DIC deformation mesh through a Python script that translates the mesh onto the finite element geometry based on four geometric characteristics. Finally, the converted deformations are mapped onto the nodes of the finite element mesh and defined as imported displacement boundary conditions. We repeat the process of measuring, processing, converting, and mapping the experimental data for a single snapshot for the definition of multiple load steps. Hence, the consecutive load steps enable the FEA of the interface debonding, based on identical experimental deformations.

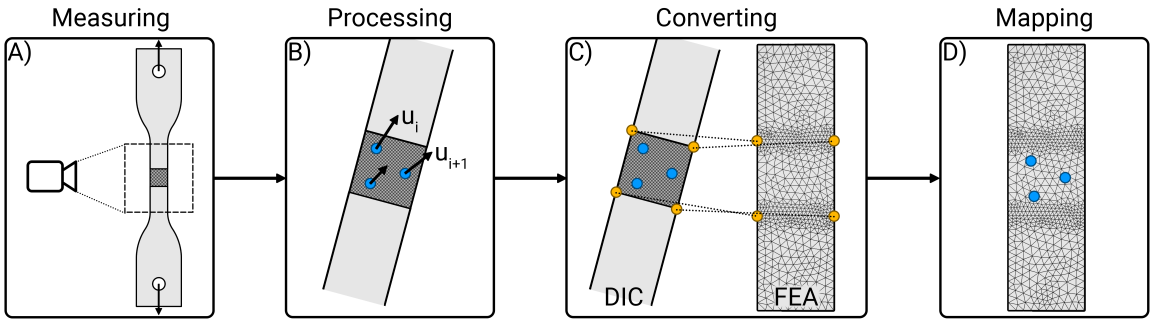

Figure 2.2: Four process steps in the digital image correlation (DIC) deformation mapping method for acquiring experimental-based local stresses. (A) Optical measurement of region of interest during loading of the sample. (B) Nodal deformations, u_i, that correlate to the deformation of the high contrast speckle pattern. All nodes combined produce the DIC deformation mesh. (C) Translation of the DIC deformation mesh according to four geometric characteristics to align it to the finite element mesh. (D) Mapping of the obtained deformations as imported nodal deformations.

To obtain the critical equivalent stress at which the interface starts to debond, we rely on the calibrated hyperelastic material (subsection 2.1.2) assigned to the finite element geometry. Its material characteristics ensure that any applied soft material strain is directly accompanied by the corresponding stress. At this stage, the FEA enables one to read the resulting stresses located at the debonding front. Doing so for multiple samples of mode I and mixed-mode failure result in a set of equivalent stress measurements at the point of debonding initiation under different loading conditions (Figure 2.1.D). The mean and standard deviation calculations of the stress measurements provide a substantial measure of when the hard-soft material interface starts to debond under a specific loading condition. This equivalent stress is what we refer to as the loading-dependent critical stress of the interface.

However, the acquired loading-dependent critical stresses of the interface merely define the debonding for two specific loading scenarios. The critical stress for any mixed-mode interface loading should be known to accurately define when debonding initiates. We, therefore, extend the range of the loading-dependent critical stresses to that of normal separation (mode I) to shear separation (mode II) via equation (2.5). This extrapolation is analogous to the common approach in mixed-mode traction-separation laws (Figure 1.1) [26], [54]. Doing so enables describing the critical stress at which debonding occurs as a function of the local loading direction, ϕ (Figure 2.1.F). We determine ϕ for every node along the length of the interface based on the dot-product of the curve and loading directional vectors, $\mathbf{C}$ and $\mathbf{L}$, respectively. We define the node-to-node directional vectors of $\mathbf{C}$ based on the nodal locations along the length of the interface. $\mathbf{L}$ contains the length normalized vector addition of the nodal principal stress magnitudes.

$$\phi = cos^{-1}(|\mathbf{C} \cdot \mathbf{L}|) = cos^{-1}\left(\frac{|x_c x_l + y_c y_l|}{\sqrt{x_c^2 + y_c^2} * \sqrt{x_l^2 + y_l^2}}\right) \tag{2.4}$$

With x_c and y_c the x- and y-vector components for the nodal curve direction and x_l and y_l the x- and y-vector components for the nodal loading direction. Note that the denominator in (4) is equal to one as the considered vectors are of unit length. Furthermore, by taking the absolute value of the dot-product, ϕ only contains values from the range of 0° to 90°. This range becomes evident once we start considering the failure mode criteria coupled with ϕ. An angle of 0° equates to tangential loading, *i.e.*, mode II, whereas a 90° equates to perpendicular loading, *i.e.*, mode I. Any angle within those two extremes is referred to as mixed-mode loading. The determined angle is crucial for the calculation of when the interface starts to debond. Commonly found in literature and implementations in commercial software, a power-law equation forms the foundation of the mixed-mode magnitude for damage initiation [26]. We consider a similar approach that determines the mixed-mode critical stress $\sigma_{M,c}$ based on ϕ, the power-law exponent α and the mode I and II critical stresses $\sigma_{\perp,c}$ and $\sigma_{\parallel,c}$, respectively:

$$\sigma_{M,c} = \sqrt[\alpha]{\frac{(\sigma_{\perp,c}\sigma_{\parallel,c})^{\alpha}}{(m_{\parallel}\sigma_{\perp,c})^{\alpha} + (m_{\perp}\sigma_{\parallel,c})^{\alpha}}} \tag{2.5}$$

With $m_{\parallel} = 1 - \frac{\phi}{90°}$ and $m_{\perp} = \frac{\phi}{90°}$. To investigate the effect of multi-material bonding on the structure's optimal joining strength, we examine two values for α. Here, $\alpha = 1$ presents a linear extrapolation, whereas $\alpha = 2$ presents a quadratic extrapolation (Figure 2.1.E). Addressing the calculation of (2.5) for every node along the length of the interface accommodates for the requirements to calculate the interface's average critical equivalent stress, which we will utilize to obtain the objective function, discussed in the following subsections.

Once we obtained the individual material characteristics and after obtaining our two hypotheses of interface failure equations, we implemented a genetic optimization algorithm for a parameterized interface.

2.2. Structural optimization algorithm

For creating the SO, we first parameterized the interface according to several constraints. Subsequently, we implemented the GA to update our interface designs according to material bonding and mechanical interlocking objectives. We will describe these aspects of SO here.

2.2.1. Parametric design

The number of design variables can drastically impact the computational expense of structural optimizations [55], [56]. Each increase in the amount of design variable exponentially adds up to the size of the solution space, *i.e.*, the number of solutions [57]. Therefore, it is preferred to maintain a low amount of design variables from an efficiency perspective. On the other hand, fewer design variables suppress the robustness of a SO [57], [58]. Each decrease in the number of design points subtracts from the size of the solution space, *i.e.*, possibly neglecting the solution that represents the global optimum for the engineering problem. In the view of robustness, it is preferred to maintain a high amount of design variables. For the current problem, we use the coordinates of four control points to define the design variables for the SO (Figure 2.1.F). Each control point contains two design variables, those for the x- and y-coordinates, except for the first control point which has its x-coordinate fixed to zero. Therefore, we consider a design variable set containing seven variables.

$$\boldsymbol{\chi} = [P_{1y}\ P_{2x}\ P_{2y}\ P_{3x}\ P_{3y}\ P_{4x}\ P_{4y}] \tag{2.6}$$

The four control points, $P_1 - P_4$, are used for the positions through which a smooth curve must cross. This curve then represents the interface, dividing the design domain into two regions of dissimilar materials. Four control points were found to provide a proper balance between efficiency and robustness. Boundaries on the design variables then enclose the solution space. We define the design variable boundaries to be 0.2 mm and 5.0 mm for the lower and upper boundaries, respectively. In addition to these boundaries, a snap-to-grid option ensures that only coordinates from a multiplicity of 0.2 mm are feasible. This option drastically reduces the number of solutions, therefore increasing efficiency. The impact on the robustness, on the other hand, is negligible as we do not differentiate between designs

that differ from each other with coordinates smaller than the snap-to-grid value.

However, the current solution space allows for the generation of designs that contain self-intersecting lines, *i.e.*, loops. We introduced several parameter relationships to ensure that any combination of design variables will result in a loopless design. These parameter relationships classify designs as infeasible if they exceed the relationship rule. The relationships are based on the directional vectors between the control points. Here, we distinguish 3- and 4-point loopless relationships, as either three or four control points can introduce loops. Figure 2.3 illustrates arbitrary curves that represent the division of half of the design domain. The 3-point loopless relationships ensure that the angle between two directional vectors set up by three consecutive control points is greater than ten degrees. This parameter relationship successfully prevents corners from self-intersecting. The 4-point loopless relationships ensure that the control points' consecutive order is not simultaneously horizontally and vertically monotonic. In other words, to prevent four control points from creating self-intersecting lines, the directional vector between points 2 and 3 must satisfy a maximum of one opposite horizontal or vertical direction with respect to the directional vector between points 1 and 4. This parameter relationship successfully limits the solution space to exclude designs that contain loops generated by four control points. All applied parameter relationships are provided mathematically in Appendix B.

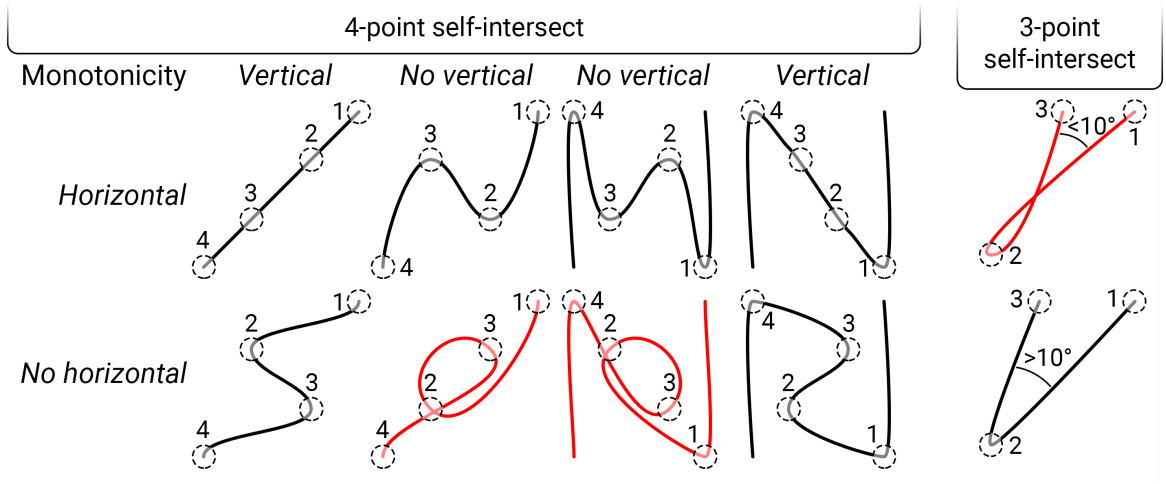

Figure 2.3: Arbitrary curves that divide half of the design domain, classified for three and four control points. The 4-point parameter relationship prevents four points from creating self-intersecting curves (bottom red lines). The 3-point parameter relationship prevents self-intersecting curves by obstructing sharp corners (top red line).

2.2.2. Objective functions

The SO's objective function defines whether a particular design is considered good or bad. The objective function value is critical in the optimization process for comparing and selecting designs. In the SO of the interface design, we focus on the joining strength of VC-A30 materials. As stated earlier, the joining strength is affected by the adhesive bond between the dissimilar materials and the extent of mechanical interlocking. Therefore, we define two objective functions.

First, the material bonding objective concerns the extent to which one material bonds to the other. Here, there is no contribution of the mechanical interlocking. The contact conditions are described by perfect bonding. Perfect bonding conditions commensurate with no penetration, no normal separation, and no tangential sliding of the two individual materials with respect to each other. These conditions allow for determining the loading direction (ϕ) at the interface when the sample is loaded. The material bonding objective is defined by the loading-dependent critical stress of the interface, $\sigma_{M,c}$, and the length of the interface, L_{tot}:

$$\max_{\boldsymbol{\chi}} f_{MB}(\boldsymbol{\chi}) = \frac{\sum_{i=1}^{n}(\sigma_{M,c,i}(\boldsymbol{\chi}) * L_i)}{L_{tot}(\boldsymbol{\chi})} \tag{2.7}$$

With $\sigma_{M,c,i}$, L_i and n the nodal loading-dependent critical stress, the length between the current and

adjacent node, and the number of nodes on the interface, respectively. We consider the average loading-dependent critical stress over the entire interface to be an adequate performance indicator of material bonding. A greater value equates to higher stress required for the entire interface to debond. To properly compare the material bonding performance among various geometries, we normalized the averaged stress to a unit of contact length. Normalizing ensures that a particular design cannot become favorable in the optimization due to the advantageous use of a greater contact length.

Secondly, the mechanical interlocking objective concerns the amount of force required to separate the individual material from each other without taking the material bonding into account. Here, we assume frictionless sliding conditions. In these conditions, normal separation and tangential sliding can occur without resistance to enable unlocking of the individual materials. The maximum force obtained for reaching an unlocked state defines the performance in mechanical interlocking. We normalize the objective function value concerning a fixed width of 75 mm as the width for the fracture samples used for validation:

$$\max_{\boldsymbol{\chi}} f_{MI}(\boldsymbol{\chi}) = \frac{F_{max}(\boldsymbol{\chi})}{75/(v(\boldsymbol{\chi}) * w(\boldsymbol{\chi}))} \tag{2.8}$$

With v the integer number of periodic repetitions of interface designs and w the interface design's width.

Both material bonding and mechanical interlocking objectives are active during the optimization of the bonded interface design. Employing dedicated FEAs in Ansys facilitates obtaining the control point-dependent values that define the objective function values. The Ansys APDL code that establishes the required data from the FEA is provided in Appendix C. The material bonding FEA comprises perfect bonding contact conditions, 0.2 mm quad interface elements and a 1 mm applied deformation loading condition. The mechanical interlocking FEA uses the identical mesh but instead further comprises frictionless contact conditions and an 8 mm applied deformation loading condition.

2.2.3. Constraints

The SO's constraint define which regions of the solution space are infeasible. In contrast to the previously mentioned parameter relationships, the constraints include values obtained from the FEA results. In other words, an applied constraint could determine a design to be infeasible, based on the design's performance. Similarly, constraints affect the solution space, but limit it to designs of interest.

In our interest to prevent a design from becoming favorable due to the arrangement of more advantageous materials, we designate a volume ratio constraint on the design (2.9). This entails that within the given design domain, the hard-to-soft material ratio is approximately equal to one. As this ratio is not dependent on the FEA's results but instead on the combination of design variables, we quantify a design's material volume ratio prior to the analysis. We approximate the area of one material by a trapezoidal method on the control point coordinates.

$$A_{14} = \sum_{i=1}^{3} \frac{P_{iy} + P_{(i+1)y}}{2} * (P_{(i+1)x - P_{ix}}) \tag{2.9}$$

For the design to satisfy the constraint, the obtained area must equal half of the area corresponding to the bounding box that encloses the interface curve. It should be noted that we allow the former area to deviate ±0.6 mm^2 from the volume constraint to prevent over-constraining.

Furthermore, we constrain the designs to those that do not show soft material damage during applied loading in the mechanical interlocking FEA. The constraint value is based on the critical equivalent strain magnitude corresponding to A30, $\sigma_{A30,c} = 1\ MPa$. This constraint successfully rules out designs that achieve infeasible magnitudes in stress due to an otherwise never-failing soft material.

2.2.4. Algorithm

Finding the global optimum can be challenging due to the size of the solution space and local optima, depending on the optimization problem. Fortunately, plenty of algorithms exist that attempt to obtain the global optimum efficiently and robustly. In this work, we make use of a GA. Figure 2.4 describes the

workflow of the algorithm. The algorithm depends on an initial set of designs, in our case a total of 128 designs with the design variables ranging between their boundaries. Each design is evaluated through a dedicated FEA for each of the objective functions $f_{MB}(\boldsymbol{\chi})$ and $f_{MI}(\boldsymbol{\chi})$. The corresponding objective function values naturally scatter the designs in a plane set up by the objective performances. We refer to the designs that dominate in this scatter as the designs at the Pareto front. The algorithm satisfies convergence when a majority of the designs in a current generation are located at the Pareto front. As we define each generation to contain twenty designs, our convergence criteria for the maximum allowable Pareto percentage of 95% means the algorithm converges if at least 19 designs of the current generation are located at the Pareto front. In addition, a convergence stability percentage of 0.2% satisfies convergence when a current generation is stable in comparison to the previous one. Here, the stability is based on the mean and standard deviation of the objective functions. A generation that did not converge is subjected to the consecutive processes of selection, crossover, and mutation. Selection defines which 20 designs are picked for reproducing with other included designs. The algorithm determines which designs to select based on the previous fitness evaluation. The selected designs then encounter crossover in which their set of designs variables recombine to generate offspring designs. The probability of crossover is 98%, implying that 2% of the selected designs avoid the crossover process and thus remain unchanged. Finally, a 10% probability of mutation alters offspring designs by varying one or more of its design variables. Mutation, therefore, generates entirely new designs with the potential of improved performance and prevents the algorithm from stagnating at any local optima. At this stage, the designs are added to the design pool. It is here where the entire process repeats iteratively until the loop exits once convergence is satisfied. In other words, the algorithm achieves the optimal interface design when no other known design can improve it.

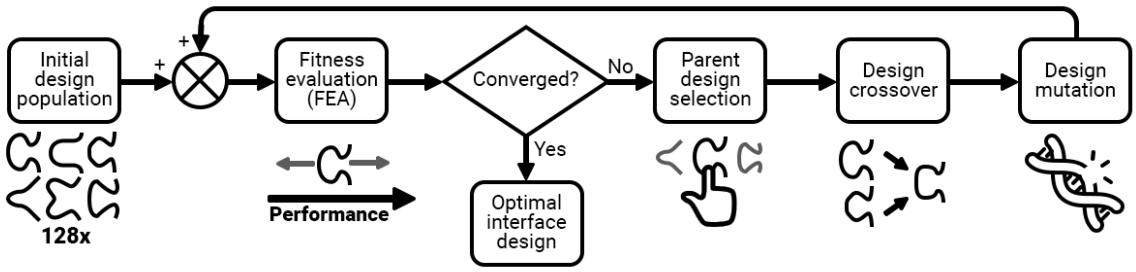

Figure 2.4: Genetic algorithm flowchart for iteratively updating the multi-material interface design.

2.3. Validation

With the methods for modeling and SO comes the requirement to validate these methods. Consequently, we introduce experimental validations that assess the characterization methods and the SO performance improvements. Dedicated validation experiments allow for comparing and contrasting of experimental and FEA results.

We validate our material models based on comparing stress-strain responses between experimental and FEA results of identical geometries and loading conditions. Analogous structural responses indicate good agreement between results and would, therefore, validate our implementation of material models. Furthermore, we reproduce a similar comparison for the validation of the interface characteristics. Here, we compare the stress-strain response at the interface originating from experimental and finite element analyses. As the interface's experimental analysis greatly relies on the DIC deformation mapping method, its validity is investigated as well. We introduce maximum interface stresses and strains to assess the correlation between the results obtained by deformation mapping and original FEM loading conditions.

The GA output provides interface designs for the fabrication of periodic A30-VC samples. Here, we briefly investigate the effect of the periodic phase on critical stress concentrations that may affect the experimental results. Therefore, we compare the interface stress distributions in two periodic inter-

face phases on non-periodic samples to illuminate its effect on the results (Figure 2.5 right). Hereafter, we asses the performance of the single f_{MI} objective SO by comparing the structural responses of optimized versus non-optimized debonded periodic interface samples. The lack of material bonding in debonded samples enables one to investigate the mechanical interlocking aspect of multi-material joints, without the effects of material bonding. Accordingly, we validate the contribution of material bonding by comparing the maximum experimental tensile stresses of debonded versus bonded samples. We assess the performance of the bonded candidate designs and the corresponding structural optimizations by introducing two experimentally measurable validation metrics. These metrics present the design's maximum tensile stress and the averaged stress along the interface. Despite their lack of direct relationship with the objective functions, the measurements represent similar joining principles in identical units. Here, the maximum tensile stress examines the magnitude of the loading vector similarly as in the mechanical interlocking objective function. The averaged interface stresses are derived identical to the material bonding objective function. These validation metrics enable one to conclude on the distinguishment between linear and quadratic interface bonding characteristics. The optimized bonded designs are then contrasted against their non-optimized counterparts to carry out validation on the SO's improving capabilities.

The experimental setup to obtain the validation variables is as follows. From the outcome of the GA, we select two optimal designs per hypothesis of failure equation, *i.e.*, a total of four optimized candidate designs. The control group consists of two non-optimized designs, generated in a primal generation of the optimization. The SO with an inactive material bonding objective provides a single optimized debonded interface design. Similar to the bonded samples, a single debonded non-optimized control design is selected from a primal design generation. We then assign each interface design to 3D printed periodic samples which we then test under tensile conditions (Figure 2.5). The individual material parts are printed in place for bonded samples, while they are printed separately for debonded samples. The non-periodic interface samples are printed to investigate the interface's side stress concentrations.

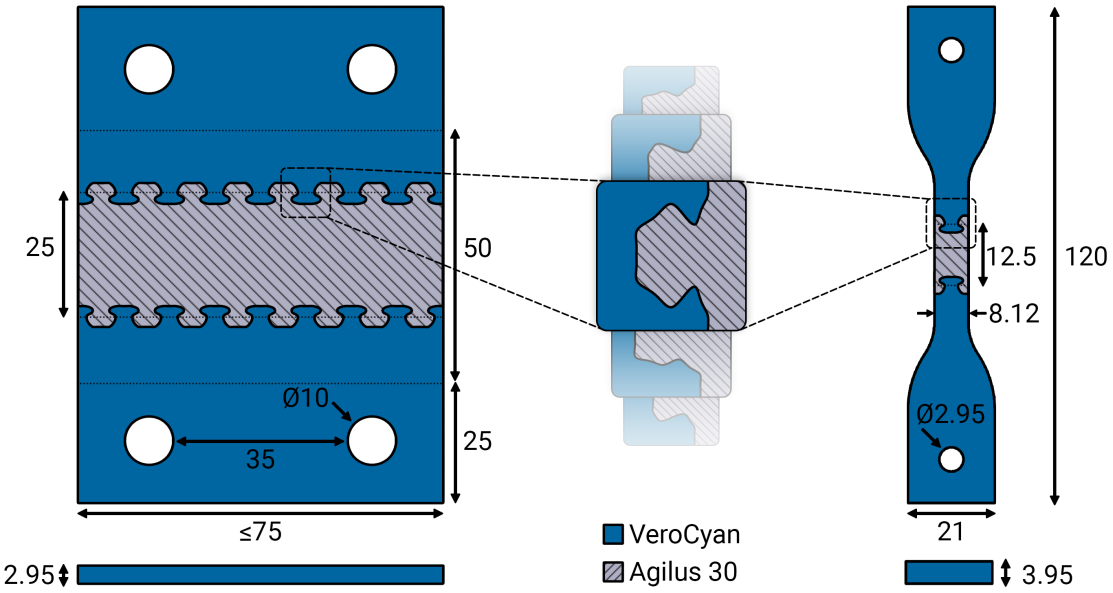

Figure 2.5: Periodic (left) and non-periodic (right) tensile samples used for experimental validation. Identical dimensions are used for different interface designs. Dimensions are in mm.

3

Results & Discussion

The current section will present and discuss the obtained results. The subsections cover the results of both individual material and interface characteristics and the optimal interface design. Furthermore, we will cover the experimental results to validate the numerical models and SO.

3.1. Material characteristics

Two separate material models approximate the individual material characteristics. The upper plot in Figure 2.1.B presents the experimental engineering stress-strain data of the VC sample. We model the hard VC material with a multilinear isotropic hardening material model. Equation (2.1) defines the non-linear plastic response by a multilinear approximation. Applying the obtained values directly to the multilinear isotropic hardening material model results in the finite element structural response of VC indicated by the dashed line in Figure 2.1.B. The correlations of determination (R^2) define to what extent the FEA results fit the experimental observations. For the structural response up to the point of yielding of VC, we find $R^2_{VC} = 97.74\%$. From these results, one can clearly observe that VC's relevant structural responses are in good agreement between experimental and numerical results. Because preliminary loading results implied induced stresses and strains far from VC's critical magnitude, we reasonably assumed one can neglect the modeling of the VC damage initiation criteria for the applications considered.

We modeled the soft A30 material with a hyperelastic Mooney-Rivlin material model. For determining the correct material constants we solely focus on the non-linear elastic behavior of the material. The solid line in the lower plot of Figure 2.1.B presents the experimental stress-strain data of the A30 sample, characterized by the elastic S-curve response recognized in literature [52]. The NLPQL optimization successfully achieves the specific combination of Mooney-Rivling material constants that provide minimal error to the experimental results: $c_{01} = 55.75$, $c_{02} = 0$, $c_{10} = 14.45$, $c_{11} = -1.044$, and $c_{20} = 0.3647\ KPa$. The dashed line indicates the corresponding numerical stress-strain response for A30 (Figure 2.1.B). By comparing the two results, one can observe the similarities in structural responses. For the structural response up to the point of yielding of A30, the correlation of determination is $R^2_{A30} = 99.91\%$, defining the Mooney-Rivlin material model to be sufficiently capable of simulating the non-linear elastic behavior of A30. Furthermore, we acquire the damage initiation criterion, the critical equivalent strain at which A30 initiates failure, based on the stress-strain data. We use this criterion as a constraint that prevents the mechanical interlocking optimization from generating designs that would be favorable with an unfeasible amount of strain. Therefore, an approximation of the damage initiation criteria suffices for its purpose. Based on the obtained structural response, we consider the A30 material to fail at an equivalent strain of 1.00 mm/mm.

3.2. Interface characteristics

The tensile loading of the interface samples (Figure 2.1.A) in combination with DIC measurements establishes the DIC deformation meshes (Figure 2.1.C) to characterize the interface. The interface

characteristics are expressed in terms of critical stress at which the bonded interface starts to debond. The local precision of DIC allows for mapping deformations such that one could obtain these local critical stresses. Under loading, A30 strains accumulated up to around 1 mm/mm, whereas the much stiffer VC remained relatively undeformed. The measurement, processing, converting and mapping of multiple consecutive DIC deformation snapshots allows for monitoring the stresses following a progressively debonded interface. The solid lines in Figure 2.1.D visualize the local equivalent stresses at the front of debonding. We present the critical debonding equivalent stresses over normalized interface lengths to compare the two loading conditions. First, we distinguish the two interface loading conditions that were tested. On average, the debonding stresses in 45 degrees mixed-mode loading are greater than those found in mode I loading of the interface. The mixed-mode loading of the interface causes debonding to occur at $\sigma_{45,c} = 1.39\ MPa$, whereas mode I loading results in debonding at $\sigma_{\perp,c} = 0.82\ MPa$. We take the mean stress measurements as a substantial measure of when the hard-soft material interface starts to debond under a specific loading condition. Furthermore, we note the location of the measured stresses along the length of the normalized interface. Despite not directly deducible from the figure, the shift in measured location along the interface corresponds to the debonding propagation over time. The slight increase in critical stresses as debonding propagates might be explained by the corresponding reduction in the contact area. Nonetheless, regardless of noise, the DIC deformation mapping method satisfies in providing an estimate of the loading-dependent critical debonding stress. Finally, the obtained critical stresses, $\sigma_{\perp,c}$ and $\sigma_{45,c}$, function as reference points in the full loading-dependent mixed-mode debonding criterion. We determine the magnitude of the critical debonding stress in mode II, $\sigma_{\parallel,c}$, with equation (3.1).

$$\sigma_{\parallel,c} = \sqrt[\alpha]{\frac{(\sigma_{45,c} m_1 \sigma_{\perp,c})^{\alpha}}{\sigma_{\perp,c}^{\alpha} - (m_2 \sigma_{45,c})^{\alpha}}} \tag{3.1}$$

Figure 2.1.E presents the linear and quadratic power law extrapolations through the measured critical stresses. As a result of investigating two values for α, we acquire two distinct debonding criteria. The linear extrapolation ($\alpha = 1$) ranges from $\sigma_{\perp,c} = 0.82\ MPa$ to $\sigma_{\parallel,c} = 4.59\ MPa$ for the critical mode I and mode II stresses, respectively. The quadratic extrapolation ($\alpha = 2$) ranges from $\sigma_{\perp,c} = 0.82\ MPa$ to $\sigma_{\parallel,c} = 1.31\ MPa$ for the critical mode I and mode II stresses, respectively. Naturally, both failure equations intersect the measured magnitudes of $\sigma_{\perp,c}$ and $\sigma_{45,c}$. However, the greater curvature of the critical stress in the quadratic extrapolation due to the higher exponent in equation (3.1) results in a smaller critical debonding stress in mode II loading. The opposite is true for the linear extrapolation, resulting in a greater critical debonding stress in mode II loading. Therefore, the latter debonding criterion also sustains greater interface stresses in the range of 45 degrees mixed-mode to tangential mode II loading. In the other end of the loading spectrum, the two debonding criteria show greater similarities, however not identical. Although critical stresses for additional loading directions would allow for a more accurate definition of α, obtaining these stresses would be out of this work's scope. As we are merely interested in assessing the effect of interface characteristics, the two failure equations allow for exactly that, regardless of the accuracy of α.

3.3. Optimal interface design

Once the individual material and interface characteristics are obtained, the definition of a parametric design sets up the requirements for the subsequent SO. However, before we assess the performance of these designs, we will briefly consider the process results of the SO that provided these designs. These results include the evolution of the objective functions in particular. They elucidate on their contribution within the joint as they represent the fundamental working principles of multi-material joining.

Figure 3.1 presents the evolutions of the individual normalized objective functions f_{MB} and f_{MI} during the optimization, with the dashed lines presenting their second-order polynomial curve fit. Equation (3.2) ensures the values for the objective functions range between zero and one for comparing and adding purposes.

$$Normalised f = \frac{f_i - min(f)}{max(f) - min(f)} \tag{3.2}$$

With f any objective function and f_i the objective function value for a single design iteration. The mean

value of the two objectives presents the total objective function value, f_T. Here, as we do not define any priority in objectives, deriving the mean suffices for determining the total objective function value. Moreover, the change of the objective functions can be observed as the design iterations evolve. Note that the values for f_{MB} and f_{MI} commonly alternate in performance among designs. In other words, for a single design, the material bonding objective could perform well while the mechanical interlocking objective does not, or vice-versa. Alternating objective function values for the designs can be observed in both optimizations with $\alpha = 1$ and $\alpha = 2$. Their alternating behavior during the evolution of designs is the first implication that material bonding and mechanical interlocking have contradicting contributions to the overall multi-material joining strength. Their evolution further illustrates this contradicting behavior of the objective functions in the quadratic bonding optimization. Despite their contradicting responses, one can observe the combined behavior for iterative designs in f_T. Here, the generational increments brought in by the GA result in improved performance for both linear and quadratic interface failure equations. However, the improvement in $\alpha = 2$ designs is only minor, whereas in $\alpha = 1$ designs it is better recognized. Each generation consists of 20 design iterations, where the optimal design candidates are obtained from the final generation, marked with green circles. Noteworthy is the number of generations required for the GA to converge. The GA took more than double the amount of generations required to find convergence in the linear bonding optimization. We explain this by the difference in locations of the global optima within the solutions space. The solution space is consistent in the two optimizations, whereas the locations of the two global optima are not. An optimization with its global optimum located closer to the set of initial solutions would result in fewer generations required to find convergence, *i.e.*, the optimization with quadratic bonding.

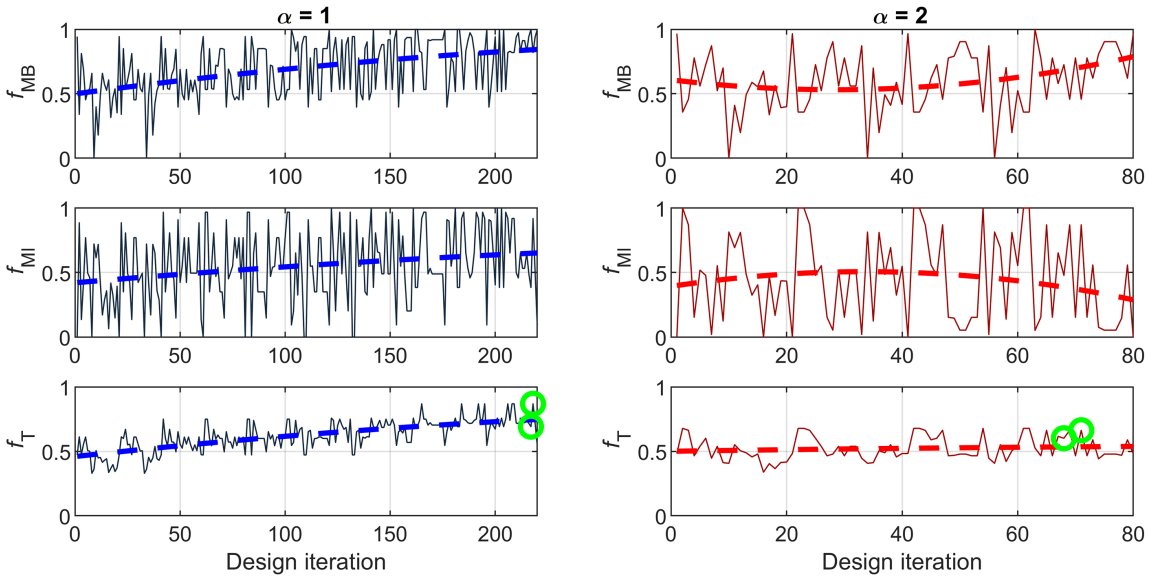

Figure 3.1: Objective function value evolutions in SO for linear (left) and quadratic (right) material bonding characteristics. f_{MB} and f_{MI} present the normalized material bonding and mechanical interlocking objective function values, respectively. The combined objective function value is presented in f_T. A second-order polynomial curve fit resembles a smoothed evolution (dashed lines). The optimal design candidates are indicated by green circles.

Furthermore, Ansys provides the sensitivity analysis on the objective functions (Figure 3.2). The sensitivity analysis describes the sign of the objective function's correlation with each of the design variables. For example, the increase of the y-coordinate of control point 1 correlates with the increase in the mechanical interlocking objective function value. Therefore, this particular sensitivity is defined as positive. Concurrently, the increase of the y-coordinate of control point 1 correlates with the decrease in the material bonding objective function value (*i.e.*, a negative sensitivity). The sensitivity magnitudes are however barely distinguishable for each design variable. The almost identical magnitude in the opposite direction implies that a design variable's attempt to improve one objective function value always comes at the expense of similar size in the other objective function value. Noteworthy is the agreement that the increase of y-coordinates benefits the joint's mechanical interlocking aspect. In contrast, the increase in x-coordinates benefits the joint's material bonding aspect. The present objective function

trade-off seems to be coupled to the horizontal and vertical displacements of the control points. Essentially, mechanical interlocking prefers more shallow, wider designs, whereas material bonding prefers narrow, deeper ones. The optimized Pareto Fronts further illustrate this objective trade-off (Figure 3.2). By contrasting the two objectives for the non-dominated designs in the final GA generation, one observes the result of the mentioned sensitivities. Again, underlining the negative correlation between the two joining principles. The observed trade-off implies that each objective function carries a priority corresponding to the contribution in joining. A proper objective priority definition would require a validation of the individual joining principles. A definition in objective priorities potentially alters the trade-off decisions made in the SO.

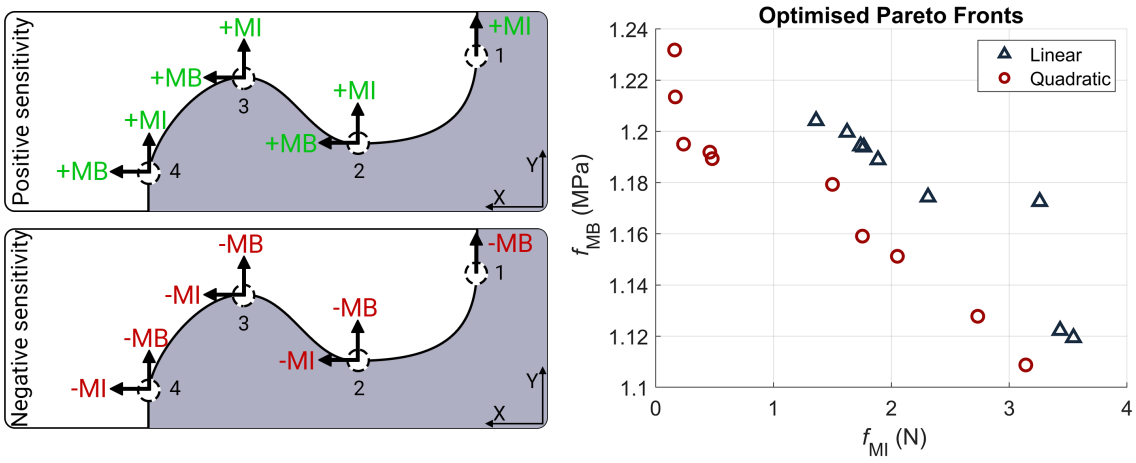

Figure 3.2: Objective function sensitivities (left) and trade-offs (right). The arrows present the design variables' increment directions, which are accompanied by their corresponding sensitivity towards the objectives of material bonding (MB) and mechanical interlocking (MI). The Pareto Fronts scatter the non-dominated designs in terms of the objective functions of material bonding (f_{MB}) and mechanical interlocking (f_{MI}) in linear and quadratic bonding optimizations.

The GA successfully provides optimal interface designs (Figure 3.3). Two candidates resemble the trade-off in joining objectives. Already, one can observe the difference in optimal design shapes as a result of distinct interface characteristics. The linear bonding designs L1 and L2 are distinguishable from the quadratic bonding designs Q1 and Q2. Compared to the control designs, the optimized designs have noticeably deeper cavities, while similar in width.

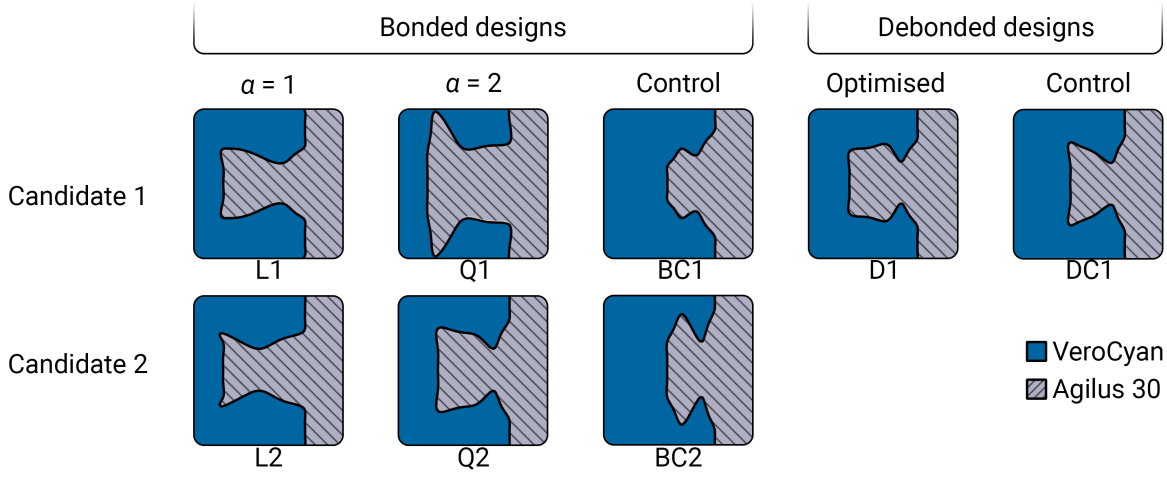

Figure 3.3: Selected genetic algorithm output designs for bonded and debonded contact conditions. Bonded contact conditions contain optimized candidate designs for linear ($\alpha = 1$) and quadratic ($\alpha = 2$) bonding and non-optimised designs (control). Debonded contact conditions contain an optimized and non-optimized (control) design.

3.4. Validation

To better validate the observations from the SO for the optimal interface geometry, we now look at the interface stresses for the optimal designs and control group. Ideally, one would want to experimentally measure the identical quantities as were utilized in the objective functions. This is challenging, and we, therefore, consider the experimentally loaded interface state using the DIC mapping method. Comparing these results to the FEM approach enables one to elucidate on the SO's modeling decisions and performance. Figure 3.4 presents the four optimized and two non-optimized bonded designs (Figure 3.3), along with their DIC and FEM stress and strain analyses at the moment of the samples' maximum tensile loading. We obtained the interface stress and strain profiles from a single center design in the periodic samples. Generally, one observes greater interface stresses at the sides of the interface design as they are located at the surface of the cavity. These stresses then reduce as the interface shapes inwards. Doing so with sharp corners achieves greater stress concentrations, visualized by both DIC and FEM loading condition results.

3.4.1. DIC deformation mapping

Before we dive into the validation of the optimized designs, we first consider the method of DIC deformation mapping for the interface characterization. From the results on the individual material characteristics in Figure 2.1.B, one can state that the material models are adequately defined to simulate the experimentally found material properties. In combination with the DIC deformation mapping, they allow for the examination of the loaded interface state (Figure 3.4). The comparison of these stresses and strains against those obtained by FEM loading conditions enables one to study the effectiveness of the DIC deformation mapping method, even for sophisticated interface designs. Both stresses and strains for the displayed six bonded designs show good agreement between DIC and FEM approaches in concentrations and overall distribution along the interfaces. The DIC deformation mapping method tends to underestimate the magnitudes with respect to its numerical counterpart, which becomes most noticeable in the interface stresses. We consider the characteristic maximum interface stresses and strains at maximum tensile loading per design to emphasize the differences in magnitudes obtained by the DIC and FEM approaches. Here, between the approaches, the correlations of determination of $R_{\sigma}^{2} = 86.36\%$ and $R_{\epsilon}^{2} = 98.17\%$ represent good agreement in stress and strain distributions, respectively, despite the mismatch in magnitudes.

The underestimation of the interface stresses by the DIC deformation mapping method emerges from the accumulated errors introduced in the process steps (Figure 2.2). First and foremost, the applied paint's limited capability to accurately represent the underlying multi-material deformations establishes thin interface gradients in the DIC deformation mesh. These gradients inaccurately represent the abrupt transition of deformations as a result of the underlying sudden change in elastic modulus. These gradients affect the interface stress read-out by mapping a deformation magnitude smaller than the actual deformation in the underlying soft material at the interface. In addition, the converting process that translates the DIC deformation mesh according to four geometric characteristics introduces further mapping error. A perfect alignment of the DIC deformation mesh onto the finite element mesh would achieve an errorless transition of deformations. However, as we define the locations of the DIC deformation mesh geometric characteristics by hand, the method is subjected to human error that negatively affects the alignment. Both the paint and converting processes illuminate the limitations of DIC deformation mapping for acquiring multi-material interface stresses. Nonetheless, these errors only seem to consistently affect the magnitude of the experimental interface stresses, rendering the stress distribution analogous to the FEM approach. Therefore, we consider the proposed DIC deformation mapping method as a valid approach to acquire multi-material interface stresses, if handled with care.

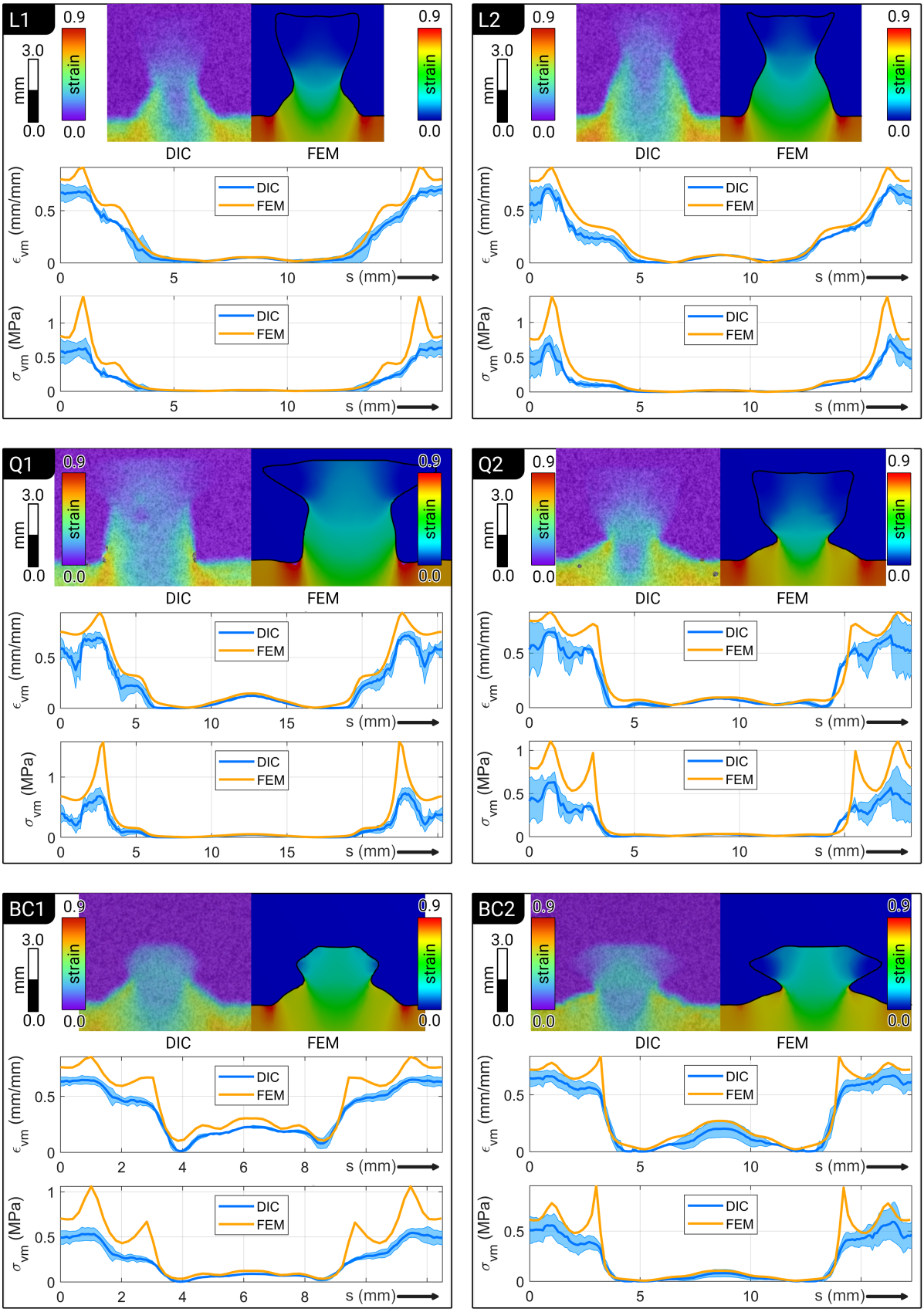

Figure 3.4: Interface stress and strain results from DIC mapping and FEM loading methods. L1 and L2 represent the linear bonded optimized designs, Q1 and Q2 the quadratic bonded optimized designs, and BC1 and BC2 the non-optimized bonded control designs. The interface measurements are taken at the maximum tensile loading of periodic samples.

3.4.2. Optimized designs

Moving on to the validation of the candidate designs, we first consider the periodic phase's effect on stress concentrations in experimental tensile tests. Our preliminary tests indicate that testing the periodic interface design without any phase shift causes critical stress concentrations at the edges of the samples. These stress concentrations develop into premature failure during tensile loading, rendering the results incompatible for design performance evaluation. As is depicted in Figure 3.5, the shifted interface contains the same design contact but is positioned differently within the tensile sample. Despite the identical contact geometry, one observes considerable differences in the interface stress distributions. Noteworthy are the stress concentrations at the sides of the samples without a phase shift. Introduced by greater shear stresses, these concentrations are not obtained in equal design regions in the shifted interface sample. The reduced stress concentrations in the shifted interface sample are observed in DIC and FEM loading condition analyses. Therefore, we continue our periodic sample validations based on half a phase shift of the interface design.

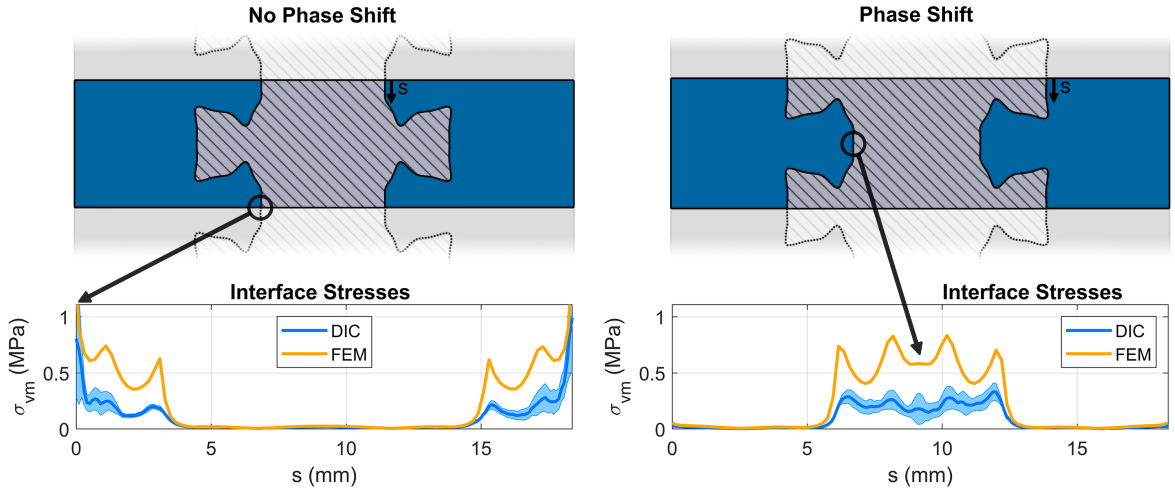

Figure 3.5: Single interface design tensile samples for no phase shift (left) and half a phase shift (right). The corresponding stresses along the interface are provided by the DIC and FEM loading condition methods. S defines the distance along the length of the interface where the circles indicate equal design regions.

Let us first consider the candidate designs obtained by the SO of the single mechanical interlocking objective f_{MI}. For the optimization of mechanical interlocking only, the designs D1 and DC1 (Figure 3.1) represent the optimized and non-optimized debonded designs, respectively. We compare the structural response of these periodic debonded designs obtained by FEA and physical experiments (Figure 3.6). Foremost, we notice the consistent underestimation of the FEA results compared to those obtained in the physical experiments. This behavior is expected as the FEA lacks contact modeling representative for the contact conditions achieved in the physical multi-material part. The latter is noticeably affected by natural friction between A30 and VC. However, in our numerical approach, we simply neglect these frictional stresses, which leads to a consistent underestimation of the samples' tensile structural response. Despite these differences, the relative performance increase is adequately estimated in the FEA. The physical experiments suggest that the optimized design performs 1.6 times better than the control design in terms of maximum tensile stress. The FEA equivalent of that performance ratio is 2.3. The reason for the FEA performance not scaling one-to-one to its physical results could again be explained by the role of the frictional contact. Here, the lack of modeling frictional stresses along the interface affects the performance approximation depending on the contact length, where a greater contact length is more subjected to these frictional stresses. Nonetheless, for approximation purposes, we can confirm the single objective's capability of adequately assessing the mechanical interlocking performance of a design.

Next, we shall consider the candidate designs obtained by the SO of both objectives f_{MB} and f_{MI}. From the SO results, we are able to distinguish optimal designs due to distinct modeling of the interface characteristics. However, to further validate the contribution of these characteristics, we introduce two

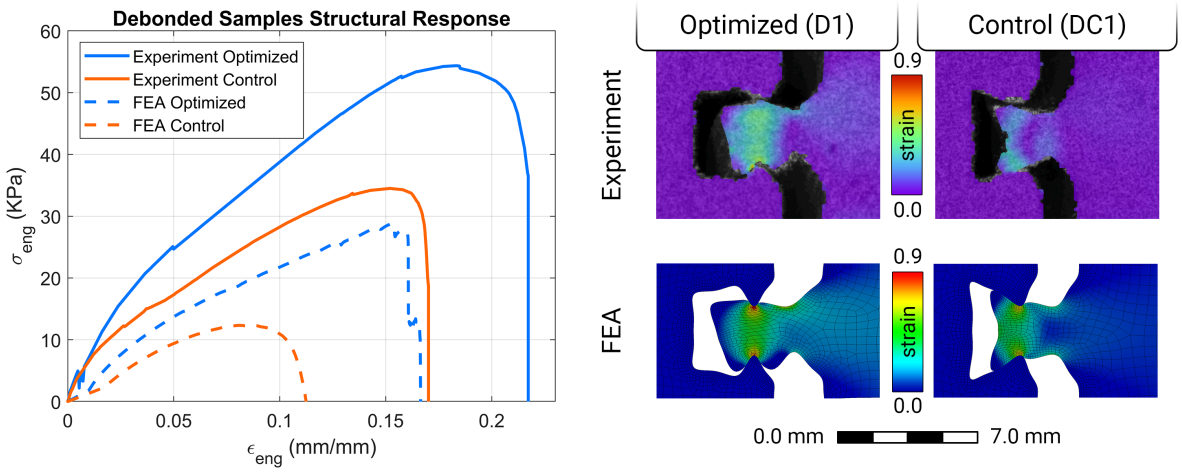

Figure 3.6: Structural response (left) of periodic debonded tensile samples with mechanical interlocking optimized (blue) and non-optimized (orange) interface designs. Loaded equivalent strain states (right) obtained from experimental and FEA results that develop into unlocked states.

measurable metrics that resemble the objective functions, *i.e.*, the multi-material joining principles. Figure 3.7 presents the maximum experimental sample stresses and average interface stresses at the maximum sample loading. In terms of maximum experimental stress, greater magnitudes correspond with better performing designs as they are able to sustain greater loads. In terms of the average interface stress, on the other hand, smaller magnitudes correspond to better performing designs as they are better capable of advantageously distributing the applied loads over the interface. By comparing the measured results in linear bonded and quadratic bonded optimized designs, distinguishing the two characteristic interface conditions becomes less evident. Concerning both validation metrics, a two-sample t-test with a significance level of 0.05 provides no statistical evidence to distinguish the considered interface failure equations. Despite the different resulting optimal designs due to distinct interface characteristics, the experimental tensile performance is statistically identical.

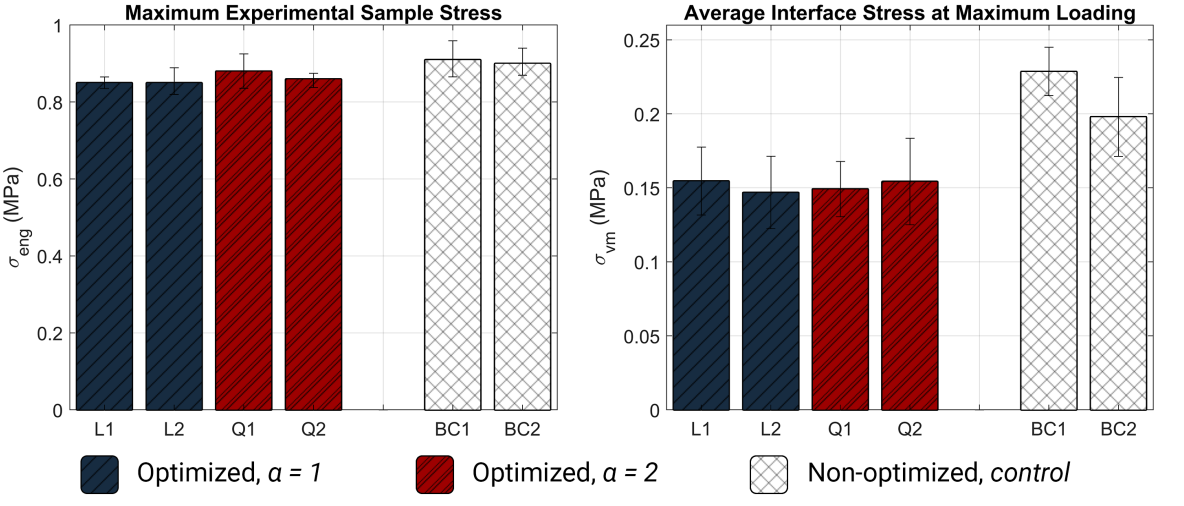

Figure 3.7: Maximum experimental sample stress (left) and average interface stress at maximum loading (right) for bonded interface candidate designs. The former is the result of the mean tensile loading of the designs, where the error bars represent a single standard deviation in uncertainty over multiple samples. The latter derives the accumulated interface stress along the interface, normalized to the design's contact length. The accumulated interface stress equates to the design's area under its stress distribution (Figure 3.4). Here, the error bars represent the single standard deviation from the mean value over the interface length. L1 and L2 are optimized with linear bonding conditions, Q1 and Q2 are optimized with quadratic bonding conditions, and BC1 and BC2 are control designs for non-optimized bonding.

Through the comparison of optimized designs and non-optimized designs, we assess the performance of the SO. Again looking at Figure 3.7, we now examine these design performances among optimal and non-optimal designs. Concerning the maximum experimental sample stress, a two-sample t-test with a significance level of 0.05 provides support for a statistical difference between the optimal and non-optimal interface designs. Surprisingly, this difference supports that the non-optimized designs can sustain greater stresses than the optimized designs. As these results suggest that the numerical improvements are not validated through the experimental testing, one may question the SO's improving capabilities. However, the results are explained by the type of failure attained in the physical experiments as opposed to those in the FEA. The physical experiments illustrate vastly different tensile failure, namely in front of the interface's soft material, remaining an intact interface. As the SO assumes that the entire interface debonds, the two results are incompatible for comparison, let alone validation. In contrast, the debonded interface samples (Figure 3.6) did show an identical failure mechanism in physical experiments and FEA. And it is for these designs that experimental mechanical interlocking is able to validate the SO mechanical interlocking objective function. However, the combined contributions of mechanical interlocking and material bonding result in a transition of tensile failure mechanism. This transition is not accounted for in the independent SO objective function analyses. The lack of accounting for the combined effect of the two joining principles sheds light on the limitations of the current SO formulation, preventing adequate validation of its improving capabilities. In short, we find that what the SO optimizes for does not adequately represent the attained failure mechanisms in physical experiments. On the other hand, the averaged stress distribution along the interface does show a considerable effect of the optimization (Figure 3.7 right). Here, the optimized designs perform noticeably better than the control designs, much more in line with the SO material bonding objective performance predictions as indicated by their common coefficient of determination $R^2_{MB} = 91.09\%$. Certainly, one may question this validation metric in the same regard as the maximum experimental stresses. However, the interface stress distribution is less subjected to the failure mechanism, making it a viable validation metric. So after all, the presented SO approach enables capable performance assessments for the individual joining principles. However, as the results also suggest, it is their combined contribution to the multi-material joint that determines the physical tensile strength. Consequently, the extent of joining principle engagements in multi-material joining becomes imperative to the interface design. In other words, one could not accurately determine the multi-material design's total joining strength based on its separated fundamental joining principles.

Earlier in section 3.3, we discussed the existing trade-off in objective functions, illustrating the contributions and priorities of the joining principles. Elaborating on this topic after physical testing, we contrast the maximum experimental sample stress for bonded and debonded designs (Figure 3.6 versus Figure 3.7 left). The combined joining principles attain stresses more than ten times greater in magnitude than those attained in interfaces that solely rely on mechanical interlocking. The considerably increased stress achieved in the bonded samples with respect to the debonded samples is a direct consequence of the addition of material bonding. Therefore, the relevancy of material bonding in A30-VC interfaces becomes evident. In these particular hard-soft material interfaces, material bonding resembles the dominant joining strategy. Accordingly, one should take this dominance into account as it affects the objectives trade-off in SO. Furthermore, as per the combination of the objectives/joining principles, the CZM enables the modeling of a debonding interface occurring alongside the material damage models. Therefore, allowing for the combination and transition of failure mechanisms underlined earlier. This work's method for defining the interface characteristics is a derivative of the CZM approach. As such, the work presented could easily be extended to include also the interface separation, *i.e.*, the implementation of a full CZM, necessary for a more accurate physical approximation of multi-material structures.

4

Conclusion

The achievement of qualitatively profound interfaces in biological multi-material structures shows the potential to provide outstanding structural performance. Today's state of engineering and research has yet to overcome the challenges encountered in multi-material design to unravel the next generation of unprecedented structural performance. With that potential in mind in this work, we break down the fundamental working principles of multi-material joining to provide greater insights into how dissimilar materials can optimally join. Here, the joining principles of material bonding and mechanical interlocking lay at the foundation of the considered A30-VC material joint.

Concerning material bonding based on realistic interface characteristics, we present an original method of DIC deformation mapping. The method successfully enables the characterization of multi-material interfaces in multiple loading conditions to account for a loading-dependent maximum traction of the interface. We achieve the interface characterization by relying solely on the traction aspect of the commonly used mixed-mode traction-separation law in CZM. Despite minor underestimations in interface stress magnitudes due to the limitations of the method, the DIC deformation mapping method shows adequate capabilities in characterizing the loading-dependent maximum traction of the hard-soft material interface. The linear and quadratic extrapolation of experimentally obtained interface characteristics provides distinguishable loading-dependent contact conditions. Using these conditions, we assess the performance of material bonding by the average loading-dependent damage initiating stress along the loaded interface. The resemblance in numerical and physical material bonding performance confirms the approach's applicability in SO.

Regarding the mechanical interlocking based on realistic material characteristics, we rely on existing FEM linear elastic and hyperelastic material models. The calibration of these models by experimentally testing the individual A30 and VC materials results in representative structural responses in the numerical environment. The consideration of a single order of magnitude in strain rate prevents the necessity of modeling the strain rate-dependent material properties in A30. Subsequently, we assess the performance of mechanical interlocking by the maximum force required to reach an unlocked state assuming frictionless contact conditions. Despite benefiting from modeling of present natural friction between A30 and VC, the approach adequately estimates an interface design's mechanical interlocking performance, making it a viable objective function in SO.

In the interest of optimizing a dissimilar material interface design for optimal joining strength, we successfully utilize a GA that guides the generational evolution of a parameterized multi-material interface design. Derived from the aforementioned multi-material joining principles, the objective of optimal joining strength achieves the combined maximization of material bonding and mechanical interlocking performances. The efficiency of the SO may differ as the interpolation of the interface characteristics affects the location of the global optimum in the solution space. From the evolution of the objective functions, one can observe opposite contributions of material bonding and mechanical interlocking to the overall joining strength, *i.e.*, a trade-off. As such, mechanical interlocking maximizes performance in more shallow, wider interface designs, whereas material bonding performs better in narrow, deeper

ones. Therefore, optimized designs encompass the trade-off in joining principles. Experimental tensile testing of these optimized designs requires thorough attention to the periodic phase to reduce the damaging effect of stress concentrations.

Conclusively, raised by our interest in how material bonding and mechanical interlocking affect the hard-soft material's optimal joining, this work's results emphasize the importance of interface conditions in multi-material structures. It is here that we find that material bonding overshadows mechanical interlocking in terms of the joining strength in A30-VC structures. Linear and quadratic bonding contact conditions show no distinguishable effect on the optimal multi-material structures' physical joining strength. However, these contact conditions do show distinct optimal designs as to how they achieve their corresponding physical joining strength. Despite adequate estimation of the individual joining principle performances, an accurate approximation of the multi-material physical joining strength necessitates the consideration of the effects induced by the interaction of material bonding and mechanical interlocking. Doing so via the CZM approach, based on realistic interface and material characteristics, enables one to achieve the optimal multi-material joining strength with an accurate embedded trade-off of joining principles.

Bibliography

[1] J. T. Haponiuk and K. Formela, *PU Polymers, Their Composites, and Nanocomposites: State of the Art and New Challenges*. Elsevier Inc., 2017, pp. 1–20, ISBN: 9780128041024. DOI: 10.1016/B978-0-12-804065-2.00001-2. [Online]. Available: http://dx.doi.org/10.1016/B978-0-12-804065-2.00001-2.

[2] J. Sun and B. Bhushan, "Hierarchical structure and mechanical properties of nacre: A review," *RSC Advances*, vol. 2, no. 20, pp. 7617–7632, 2012, ISSN: 20462069. DOI: 10.1039/c2ra20218b.

[3] M. Rousseau, E. Lopez, P. Stempflé, *et al.*, "Multiscale structure of sheet nacre," *Biomaterials*, vol. 26, no. 31, pp. 6254–6262, 2005, ISSN: 01429612. DOI: 10.1016/j.biomaterials.2005.03.028.

[4] J. M. Gosline, M. E. DeMont, and M. W. Denny, "The structure and properties of spider silk," *Endeavour*, vol. 10, no. 1, pp. 37–43, 1986, ISSN: 01609327. DOI: 10.1016/0160-9327(86)90049-9.

[5] J. O. Akindoyo, M. D. Beg, S. Ghazali, M. R. Islam, N. Jeyaratnam, and A. R. Yuvaraj, "Polyurethane types, synthesis and applications-a review," *RSC Advances*, vol. 6, no. 115, pp. 114 453–114 482, 2016, ISSN: 20462069. DOI: 10.1039/c6ra14525f.

[6] A. Khayer Dastjerdi, R. Rabiei, and F. Barthelat, "The weak interfaces within tough natural composites: Experiments on three types of nacre," *Journal of the Mechanical Behavior of Biomedical Materials*, vol. 19, pp. 50–60, 2013, ISSN: 17516161. DOI: 10.1016/j.jmbbm.2012.09.004. [Online]. Available: http://dx.doi.org/10.1016/j.jmbbm.2012.09.004.

[7] K. M. Zia, S. Anjum, M. Zuber, M. Mujahid, and T. Jamil, "Synthesis and molecular characterization of chitosan based polyurethane elastomers using aromatic diisocyanate," *International Journal of Biological Macromolecules*, vol. 66, pp. 26–32, 2014, ISSN: 18790003. DOI: 10.1016/j.ijbiomac.2014.01.073. [Online]. Available: http://dx.doi.org/10.1016/j.ijbiomac.2014.01.073.

[8] Z. Rafiee and V. Keshavarz, "Synthesis and characterization of polyurethane/microcrystalline cellulose bionanocomposites," *Progress in Organic Coatings*, vol. 86, pp. 190–193, 2015, ISSN: 03009440. DOI: 10.1016/j.porgcoat.2015.05.013. [Online]. Available: http://dx.doi.org/10.1016/j.porgcoat.2015.05.013.

[9] J. Jahn, M. Weber, J. Boehner, and R. Steinhilper, "Assessment Strategies for Composite-metal Joining Technologies-A Review," *Procedia CIRP*, vol. 50, pp. 689–694, 2016, ISSN: 22128271. DOI: 10.1016/j.procir.2016.05.034.

[10] I. Gibson, D. Rosen, and B. Stucker, *Additive Manufacturing Technologies: 3D Printing, Rapid Prototyping, and Direct Digital Manufacturing*, 2. New York, NY: Springer New York, 2015, ISBN: 978-1-4939-2113-3. DOI: 10.1007/978-1-4939-2113-3{_}1. [Online]. Available: http://link.springer.com/10.1007/978-1-4939-2113-3_1.

[11] T. D. Ngo, A. Kashani, G. Imbalzano, K. T. Nguyen, and D. Hui, "Additive manufacturing (3D printing): A review of materials, methods, applications and challenges," *Composites Part B: Engineering*, vol. 143, no. February, pp. 172–196, 2018, ISSN: 13598368. DOI: 10.1016/j.compositesb.2018.02.012. [Online]. Available: https://doi.org/10.1016/j.compositesb.2018.02.012.

[12] A. Bandyopadhyay and B. Heer, "Additive manufacturing of multi-material structures," *Materials Science and Engineering R: Reports*, vol. 129, no. March, pp. 1–16, 2018, ISSN: 0927796X. DOI: 10.1016/j.mser.2018.04.001. [Online]. Available: https://doi.org/10.1016/j.mser.2018.04.001.

[13] J. Mueller, K. Shea, and C. Daraio, “Mechanical properties of parts fabricated with inkjet 3D printing through efficient experimental design,” *Materials and Design*, vol. 86, pp. 902–912, 2015, ISSN: 18734197. DOI: 10.1016/j.matdes.2015.07.129. [Online]. Available: http://dx.doi.org/10.1016/j.matdes.2015.07.129.

[14] Y. Zheng, W. Zhang, D. M. B. Lopez, and R. Ahmad, “Scientometric analysis and systematic review of multi-material additive manufacturing of polymers,” *Polymers*, vol. 13, no. 12, 2021, ISSN: 20734360. DOI: 10.3390/polym13121957.

[15] A. Tits and D. Ruffoni, “Joining soft tissues to bone: Insights from modeling and simulations,” *Bone Reports*, vol. 14, no. December 2020, p. 100 742, 2021, ISSN: 23521872. DOI: 10.1016/j.bonr.2020.100742. [Online]. Available: https://doi.org/10.1016/j.bonr.2020.100742.

[16] R. Desmorat and F. A. Leckie, “Singularities in bi-materials: Parametric study of an isotropic/anisotropic joint,” *European Journal of Mechanics, A/Solids*, vol. 17, no. 1, pp. 33–52, 1998, ISSN: 09977538. DOI: 10.1016/S0997-7538(98)80062-4.

[17] Y. Liu, V. Birman, C. Chen, S. Thomopoulos, and G. M. Genin, “Mechanisms of bimaterial attachment at the interface of tendon to bone,” *Journal of Engineering Materials and Technology, Transactions of the ASME*, vol. 133, no. 1, pp. 1–8, 2011, ISSN: 00944289. DOI: 10.1115/1.4002641.

[18] F. Liu, T. Li, X. Jiang, Z. Jia, Z. Xu, and L. Wang, “The effect of material mixing on interfacial stiffness and strength of multi-material additive manufacturing,” *Additive Manufacturing*, vol. 36, no. August, 2020, ISSN: 22148604. DOI: 10.1016/j.addma.2020.101502.

[19] O. Zienkiewicz, R. Taylor, and J. Zhu, “Finite Element Method for Solid and Structural Mechanics,” no. 1, pp. 6–8, 2005.

[20] M. Ashby, H. Shercliff, and D. Cebon, *Materials: engineering, science, processing and design*, 3. 2010, vol. 13, p. 67, ISBN: 9780750683913. DOI: 10.1016/s1369-7021(10)70042-0.

[21] D. Wäppling, J. Gunnars, and P. Ståhle, “Crack growth across a strength mismatched bimaterial interface,” *International Journal of Fracture*, vol. 89, no. 3, pp. 223–243, 1998, ISSN: 03769429. DOI: 10.1023/A:1007493028039.

[22] P. Liu, Y. Luo, and Z. Kang, “Multi-material topology optimization considering interface behavior via XFEM and level set method,” *Computer Methods in Applied Mechanics and Engineering*, vol. 308, no. June, pp. 113–133, 2016, ISSN: 00457825. DOI: 10.1016/j.cma.2016.05.016. [Online]. Available: http://dx.doi.org/10.1016/j.cma.2016.05.016.

[23] R. Behrou, M. Lawry, and K. Maute, “Level set topology optimization of structural problems with interface cohesion,” *International Journal for Numerical Methods in Engineering*, vol. 112, no. 8, pp. 990–1016, Nov. 2017, ISSN: 10970207. DOI: 10.1002/nme.5540.

[24] C. Shet and N. Chandra, “Analysis of energy balance when using Cohesive Zone Models to simulate fracture processes,” *Journal of Engineering Materials and Technology, Transactions of the ASME*, vol. 124, no. 4, pp. 440–450, 2002, ISSN: 00944289. DOI: 10.1115/1.1494093.

[25] C. Zhang, N. Li, W. Wang, W. K. Binienda, and H. Fang, “Progressive damage simulation of triaxially braided composite using a 3D meso-scale finite element model,” *Composite Structures*, vol. 125, pp. 104–116, 2015, ISSN: 02638223. DOI: 10.1016/j.compstruct.2015.01.034. [Online]. Available: http://dx.doi.org/10.1016/j.compstruct.2015.01.034.

[26] H. Khoramishad, M. Hamzenejad, and R. S. Ashofteh, “Characterizing cohesive zone model using a mixed-mode direct method,” *Engineering Fracture Mechanics*, vol. 153, pp. 175–189, 2016, ISSN: 00137944. DOI: 10.1016/j.engfracmech.2015.10.045. [Online]. Available: http://dx.doi.org/10.1016/j.engfracmech.2015.10.045.

[27] O. M. Querin, M. Victoria, C. A. Gordoa, R. Ansola, and P. Martí, *Topology design methods for structural optimization*. Butterworth-Heinemann, 2017, ISBN: 0080999891.

[28] Y. Sui and X. Peng, *Modeling, Solving and Application for Topology Optimization of Continuum Structures: ICM Method Based on Step Function*. Butterworth-Heinemann, 2017, ISBN: 0128126566.

[29] M. P. Bensϕe and O. Sigmund, *Topology optimization theory, method and applications*, 2003.

[30] G. I. N. Rozvany, "Aims, scope, basic concepts and methods of topology optimization," in *Topology optimization in structural mechanics*, Springer, 1997, pp. 1–55.

[31] M. h. Wang, G. q. Xiao, Z. Li, and J. q. Wang, "Shape optimization methodology of clinching tools based on Bezier curve," *International Journal of Advanced Manufacturing Technology*, vol. 94, no. 5-8, pp. 2267–2280, Feb. 2018, ISSN: 14333015. DOI: 10.1007/s00170-017-0987-5.

[32] M. A. Monn, J. C. Weaver, T. Zhang, J. Aizenberg, and H. Kesari, "New functional insights into the internal architecture of the laminated anchor spicules of Euplectella aspergillum," *Proceedings of the National Academy of Sciences of the United States of America*, vol. 112, no. 16, pp. 4976–4981, 2015, ISSN: 10916490. DOI: 10.1073/pnas.1415502112.

[33] A. L. Ingram and A. R. Parker, "Structure, mechanism and mechanical properties of pupal attachment in Greta oto (Lepidoptera: Nymphalidae: Ithomiinae)," *Entomological Science*, vol. 9, no. 1, pp. 109–120, 2006, ISSN: 13438786. DOI: 10.1111/j.1479-8298.2006.00158.x.

[34] B. Melzer, T. Steinbrecher, R. Seidel, O. Kraft, R. Schwaiger, and T. Speck, "The attachment strategy of English ivy: A complex mechanism acting on several hierarchical levels," *Journal of the Royal Society Interface*, vol. 7, no. 50, pp. 1383–1389, 2010, ISSN: 17425662. DOI: 10.1098/rsif.2010.0140.

[35] J. H. Dirks and D. Taylor, "Veins improve fracture toughness of insect wings," *PLoS ONE*, vol. 7, no. 8, 2012, ISSN: 19326203. DOI: 10.1371/journal.pone.0043411.

[36] M. A. Kasapi and J. M. Gosline, "Design complexity and fracture control in the equine hoof wall," *Journal of Experimental Biology*, vol. 200, no. 11, pp. 1639–1659, 1997, ISSN: 00220949.

[37] G. Couegnat, S. L. Fok, J. E. Cooper, and A. J. Qualtrough, "Structural optimization of dental restorations using the principle of adaptive growth," *Dental Materials*, vol. 22, no. 1, pp. 3–12, Jan. 2006, ISSN: 01095641. DOI: 10.1016/j.dental.2005.04.003.

[38] L. Shi, A. S. Fok, and A. Qualtrough, "A two-stage shape optimization process for cavity preparation," *Dental Materials*, vol. 24, no. 11, pp. 1444–1453, Nov. 2008, ISSN: 01095641. DOI: 10.1016/j.dental.2008.03.016.

[39] A. Moussa, S. Rahman, M. Xu, M. Tanzer, and D. Pasini, "Topology optimization of 3D-printed structurally porous cage for acetabular reinforcement in total hip arthroplasty," *Journal of the Mechanical Behavior of Biomedical Materials*, vol. 105, May 2020, ISSN: 18780180. DOI: 10.1016/j.jmbbm.2020.103705.

[40] R. G. Balijepalli, M. R. Begley, N. A. Fleck, R. M. McMeeking, and E. Arzt, "Numerical simulation of the edge stress singularity and the adhesion strength for compliant mushroom fibrils adhered to rigid substrates," *International Journal of Solids and Structures*, vol. 85-86, pp. 160–171, 2016, ISSN: 00207683. DOI: 10.1016/j.ijsolstr.2016.02.018. [Online]. Available: http://dx.doi.org/10.1016/j.ijsolstr.2016.02.018.

[41] A. Klarbring, B. Torstenfelt, U. Edlund, P. Schmidt, K. Simonsson, and H. Ansell, "Minimizing crack energy release rate by topology optimization," *Structural and Multidisciplinary Optimization*, vol. 58, no. 4, pp. 1695–1703, Oct. 2018, ISSN: 16151488. DOI: 10.1007/s00158-018-1989-0.

[42] C. Li and I. Y. Kim, "Multi-material topology optimization for automotive design problems," *Proceedings of the Institution of Mechanical Engineers, Part D: Journal of Automobile Engineering*, vol. 232, no. 14, pp. 1950–1969, 2018, ISSN: 09544070. DOI: 10.1177/0954407017737901.

[43] C. F. Hilchenbach and E. Ramm, "Optimization of multiphase structures considering damage," *Structural and Multidisciplinary Optimization*, vol. 51, no. 5, pp. 1083–1096, 2015, ISSN: 16151488. DOI: 10.1007/s00158-014-1198-4.

[44] M. Lawry and K. Maute, "Level set topology optimization of problems with sliding contact interfaces," *Structural and Multidisciplinary Optimization*, vol. 52, no. 6, pp. 1107–1119, 2015, ISSN: 16151488. DOI: 10.1007/s00158-015-1301-5.

[45] Y. LIU, D. MATSUNAKA, M. SHIMODA, and Y. SHIBUTANI, "Interface shape design of multi-material structures for delamination strength," *Mechanical Engineering Journal*, vol. 3, no. 1, pp. 15–00 360, 2016, ISSN: 2187-9745. DOI: 10.1299/mej.15-00360.

[46] S. Graziosi, F. Cannazza, M. Vedani, A. Ratti, F. Tamburrino, and M. Bordegoni, “Design and testing of an innovative 3D-printed metal-composite junction,” *Additive Manufacturing*, vol. 36, no. October 2019, p. 101 311, 2020, ISSN: 22148604. DOI: 10.1016/j.addma.2020.101311. [Online]. Available: https://doi.org/10.1016/j.addma.2020.101311.

[47] “Theory Reference,” in *Ansys® Academic Research Mechanical, Release 19.2, Help System*, 2019.

[48] *Defining the constitutive response of cohesive elements using a traction-separation description*. [Online]. Available: https://abaqus-docs.mit.edu/2017/English/SIMACAEELMRefMap/simaelm-c-cohesivebehavior.htm#hj-top.

[49] A. Perduta and R. Putanowicz, *Comparison of elastomer modelling in various FEM packages*, 2015. DOI: 10.1016/j.proeng.2015.06.113. [Online]. Available: https://www.scopus.com/inward/record.uri?eid=2-s2.0-84939620571&doi=10.1016%2Fj.proeng.2015.06.113&partnerID=40&md5=1f6be0c5a5bd7ca9594ea1e85bcecd5c.

[50] H. Ladjal, J. Azencot, M. Beuve, P. Giraud, J. M. Moreau, and B. Shariat, *Biomechanical modeling of the respiratory system: Human diaphragm and thorax*, 2015. DOI: 10.1007/978-3-319-15503-6{_}10. [Online]. Available: https://www.scopus.com/inward/record.uri?eid=2-s2.0-84943789468&doi=10.1007%2F978-3-319-15503-6_10&partnerID=40&md5=373aeb343ca895ed3e7c029cb0b3178d.

[51] D. Amodio, G. Palmieri, and M. Sasso, *Mechanical behavior of elastomers: Experimental determination and numerical modeling*, 2013.

[52] F. F. Abayazid and M. Ghajari, “Material characterisation of additively manufactured elastomers at different strain rates and build orientations,” *Additive Manufacturing*, vol. 33, no. December 2019, p. 101 160, 2020, ISSN: 22148604. DOI: 10.1016/j.addma.2020.101160. [Online]. Available: https://doi.org/10.1016/j.addma.2020.101160.

[53] M. Hossain and Z. Liao, “An additively manufactured silicone polymer: Thermo-viscoelastic experimental study and computational modelling,” *Additive Manufacturing*, vol. 35, Oct. 2020, ISSN: 22148604. DOI: 10.1016/j.addma.2020.101395.

[54] M. Jung Lee, T. Min Cho, W. Seock Kim, B. Chai Lee, and J. Ju Lee, “Determination of cohesive parameters for a mixed-mode cohesive zone model,” *International Journal of Adhesion and Adhesives*, vol. 30, no. 5, pp. 322–328, 2010, ISSN: 01437496. DOI: 10.1016/j.ijadhadh.2009.10.005. [Online]. Available: http://dx.doi.org/10.1016/j.ijadhadh.2009.10.005.

[55] M. Zhou and G. I. Rozvany, “DCOC: An optimality criteria method for large systems Part I: theory,” *Structural Optimization*, vol. 5, no. 1-2, pp. 12–25, 1992, ISSN: 09344373. DOI: 10.1007/BF01744690.

[56] M. J. De Ruiter and F. Van Keulen, “Topology optimization using a topology description function,” *Structural and Multidisciplinary Optimization*, vol. 26, no. 6, pp. 406–416, 2004, ISSN: 1615147X. DOI: 10.1007/s00158-003-0375-7.

[57] O. Sigmund, “On the usefulness of non-gradient approaches in topology optimization,” *Structural and Multidisciplinary Optimization*, vol. 43, no. 5, pp. 589–596, 2011, ISSN: 1615-147X.

[58] P. Tanskanen, “The evolutionary structural optimization method: Theoretical aspects,” *Computer Methods in Applied Mechanics and Engineering*, vol. 191, no. 47-48, pp. 5485–5498, 2002, ISSN: 00457825. DOI: 10.1016/S0045-7825(02)00464-4.

A

DIC deformation mapping

We export the DIC evaluated data from Istra4D in .hdf5 file format for each evaluated step. The .hdf5 file format stores data hierarchically and supports to be post processed in software like MATLAB. Each step, i.e., snapshot, contains data on the local x- and y-displacments. As a result from different coordinate systems between the experiment and the FEA, the exported DIC data requires a conversion. For this conversion, the following data is required:

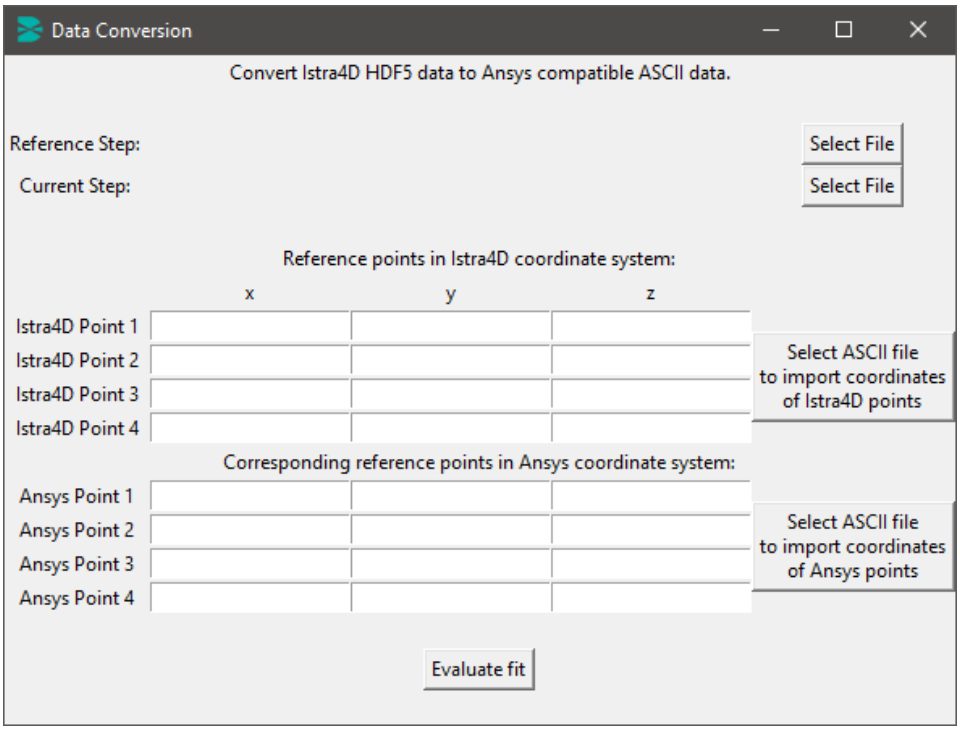

Figure A.1: DIC data conversion tool

1. Snapshot of the reference step. The selected step functions as the original state of the DIC mesh locations and corresponding deformations. Setting this step to be equal to the reference step in the DIC evaluation results in a mesh with initial deformations of zero magnitude.
2. Snapshot of the current step. This step refers to the deformed state of the DIC mesh. Here, we specify the step at which the debonding initates.
3. The coordinates in the experimental coordinate system of four reference points. We define these references points by creating gauges at characteristic locations on the DIC evaluated data.

4. The coordinates in the FEA coordinate system of the same four reference points.

Once all data is collected, we make use of a Python script to translate the DIC data onto the finite element geometry. The script evaluates the fit of the DIC data in terms of error between the coordinates of the four reference points. Once we evaluated the fit, the scripts writes the translated data into a text file.

Subsequently, Ansys reads the text data in an “external data” module. Here, we define the columns that correspond to the x- and y- coordinates and the corresponding x- and y-displacements. We then link this data to the solution section of the “static structural” module. This enables Ansys to utilize the displacement data as an imported displacement for a boundary condition. The imported displacement boundary conditions maps the displacement data onto the nodes of the finite element mesh. Note that nodes of the DIC displacement mesh do not perfectly line up with the nodes of the finite element mesh. As a result, the process of mapping the data extrapolates the DIC displacement magnitudes nearest to the finite element mesh node to determine the applied nodal displacement. In areas where there is a lack of DIC displacement data, i.e., gaps in the mesh, the Ansys mapping options allow for a filling of these gaps through extrapolation. The same applies to the extrapolation of displacement data for the outer areas that are not covered by the DIC mesh. We repeat the entire process of reading, converting and mapping the data for a single snapshot such that the deformations of the complete interface debonding are captured. Therefore, the final applied deformation consists of multiple loadsteps with corresponding snapshots that represent the interface debonding.

The definition of a construction path allows for reading the equivalent stress data along the interface once all load steps are simulated. As the path provides results over the entire interface, one cannot directly deduce the critical stress magnitude at the location where the interface starts to debond. For this, we first define the location of the debonding front for each of the considered snapshots, expressed in the distance along the interface path. We achieve this by utilizing Adobe Photoshop’s built-in measurement tool that allows for the translation of measured pixels into units of length. We define the pixel-to-mm scale based on multiple characteristic locations of the geometry. Subsequently, we read the magnitude of the equivalent stress at these distances along the interface for all snapshots. As a current distance of the debonding front does not always line up with the finite element mesh nodes, we linearly extrapolate between the neighboring nodes to define the stress more accurately. Doing so for multiple samples of mode I and mixed mode failure, results in a set of equivalent stress measurements at the point of debonding initiation under different loading conditions. The mean and standard deviation calculations of the stress measurements provide a substantial measure of when the hard-soft material interface starts to debond under a specific loading condition. This equivalent stress is what we refer to as the loading-dependent critical stress of the interface.

B

Parameter relationships

Parameter relationships constrain the design solution space to exclude undesired designs from the SO.

The following parameter relationships establish a minimal distance of 0.2 mm between the control points:

$$\sqrt{(P_{3x} - P_{4x})^2 + (P_{3y} - P_{4y})^2} \geq 0.2\ mm$$
$$\sqrt{(P_{2x} - P_{3x})^2 + (P_{2y} - P_{3y})^2} \geq 0.2\ mm$$
$$\sqrt{(P_{1x} - P_{2x})^2 + (P_{1y} - P_{2y})^2} \geq 0.2\ mm$$

The following parameter relationships prevent four control points from generating self-intersecting interface lines.

$$(P_{1x} - P_{4x}) * (P_{2x} - P_{3x}) + (-P_{1y} + P_{4y}) * (-P_{2y} + P_{3y}) \geq 0\ mm^2$$
$$(P_{2x} - P_{4x}) * (P_{3x} - P_{4x}) + (-P_{2y} - P_{4y}) * (-P_{3y} + P_{4y}) \geq 0\ mm^2$$

The following parameter relationships prevent three control points from generating self-intersecting interface lines.

$$acos\left(\frac{((2*(max(P_{1y},P_{2y},P_{3y},P_{4y})+1[mm])-P_{1y})-P_{1y})*(P_{2y}-P_{1y})}{((2*(max(P_{1y},P_{2y},P_{3y},P_{4y})+1)-P_{1y})-P_{1y})*\sqrt{(P_{2x}-P_{1x})^2+(P_{2y}-P_{1y})^2}}\right) \geq 10\ deg$$
$$acos\left(\frac{(P_{1x}-P_{2x})*(P_{3x}-P_{2x})+(P_{1y}-P_{2y})*(P_{3y}-P_{2y})}{\sqrt{(P_{1x}-P_{2x})^2+(P_{1y}-P_{2y})^2}*\sqrt{(P_{3x}-P_{2x})^2+(P_{3y}-P_{2y})^2}}\right) \geq 10\ deg$$
$$acos\left(\frac{(P_{2x}-P_{3x})*(P_{4x}-P_{3x})+(P_{2y}-P_{3y})*(P_{4y}-P_{3y})}{\sqrt{(P_{2x}-P_{3x})^2+(P_{2y}-P_{3y})^2}*\sqrt{(P_{4x}-P_{3x})^2+(P_{4y}-P_{3y})^2}}\right) \geq 10\ deg$$
$$acos\left(\frac{(P_{3y}-P_{4y})*((-P_{4y})-P_{4y})}{\sqrt{(P_{3x}-P_{4x})^2+(P_{3y}-P_{4y})^2}*\sqrt{((-P_{4y})-P_{4y})^2}}\right) \geq 10\ deg$$

The following parameter relationships establish a hard-to-soft material volume ratio within the design domain.

$$\frac{P_{1y}+P_{2y}}{2*(P_{2x}-P_{1x})} + \frac{P_{2y}+P_{3y}}{2*(P_{3x}-P_{2x})} + \frac{P_{3y}+P_{4y}}{2*(P_{4x}-P_{3x})} \leq 0.5 * ((max(P_{1y}, P_{2y}, P_{3y}, P_{4y}) + 1) * P_{4x}) + 0.6$$
$$\frac{P_{1y}+P_{2y}}{2*(P_{2x}-P_{1x})} + \frac{P_{2y}+P_{3y}}{2*(P_{3x}-P_{2x})} + \frac{P_{3y}+P_{4y}}{2*(P_{4x}-P_{3x})} \geq 0.5 * ((max(P_{1y}, P_{2y}, P_{3y}, P_{4y}) + 1) * P_{4x}) - 0.6$$

C

APDL command code

The following APDL code obtains the necessary FEA results to derive the corresponding objective function values:

```
!   Commands inserted into this file will be executed immediately after the ANSYS /POST1 command.

!   Active UNIT system in Workbench when this object was created:  Metric (mm, kg, N, s, mV, mA)
!   NOTE:  Any data that requires units (such as mass) is assumed to be in the consistent solver unit system.
!               See Solving Units in the help system for more information.


PARRES,new,parm_pro

Mean=0
Stdv = 0
Stress = 0

*VMASK,NMASK(1)
*VSCFUN,Length,SUM,NARRAY_LOC(1,7)
*VMASK,NMASK(1)
*VSCFUN,Mean,MEAN,NARRAY_PR(1,1)                    !mean calculation
*VMASK,NMASK(1)
*VSCFUN,Stdv,STDV,NARRAY_PR(1,1)                    !std. calculation
*VMASK,NMASK(1)
*VSCFUN,Stress,MAX,NARRAY_PR(1,1)                     !max principal stress calculation
*VMASK,NMASK_SOFT(1)
*VSCFUN,Strain,MAX,NARRAY_SOFT(1,1)                     !max principal strain calculation

my_Length = Length
my_Perfomance = Sigma_crit_tot
my_Mean = Mean
my_Stdv = Stdv
my_Stress = Stress
my_Time = current_time
my_Strain = Strain

my_Interface = NARRAY_DE_INT(1)
my_Soft = NARRAY_DE_SOFT(1)

```

Figure C.1: Ansys APDL command snippet to acquire objective function values.

The following APDL code calculates the critical interface stress of a loaded bonded interface:

```
!   Commands inserted into this file will be executed just prior to the ANSYS SOLVE command.
!   These commands may supersede command settings set by Workbench.

!   Active UNIT system in Workbench when this object was created:  Metric (mm, kg, N, s, mV, mA)
!   NOTE:  Any data that requires units (such as mass) is assumed to be in the consistent solver unit system.
!               See Solving Units in the help system for more information.


/com, ################################################
/com, ###Critical interface stresses

OUTRES,all,all

*GET,current_loadstep,ACTIVE,,SET,LSTP   ! current load step number
*GET,current_substep,ACTIVE,,SET,SBST    ! current substep number
*GET,current_time,ACTIVE,,SET,TIME       ! current time

*IF,current_loadstep,GT,0,then           ! after first load step SOLVE
/POST1
SET,last

*GET,NNUMMAX,node,,num,max
*DEL,ALL
*DIM,NMASK,array,NNUMMAX
*DIM,NMASK_SOFT,array,NNUMMAX
*DIM,NARRAY,array,NNUMMAX           !node array
*DIM,NARRAY_LOC,array,NNUMMAX,7     !location arrays
*DIM,NARRAY_S,array,NNUMMAX,6       !stress arrays
*DIM,NARRAY_EU,array,NNUMMAX,4      !euler angles arrays
*DIM,NARRAY_PR,array,NNUMMAX,4      !principal stress arrays
*DIM,NARRAY_PR1,array,NNUMMAX,3     !first principal stress vector arrays
*DIM,NARRAY_TAN,array,NNUMMAX,3     !curve tangent vector arrays
*DIM,NARRAY_PLV,array,NNUMMAX,3     !principal load vector arrays
*DIM,NARRAY_ANG,array,NNUMMAX,3     !curve-load and principal-vm angle array
*DIM,NARRAY_VM,array,NNUMMAX,6      !von-mises direction vector and length array
*DIM,NARRAY_CRIT,array,NNUMMAX,11   !calculation arrays including the damage criteria
*DIM,NARRAY_DIC,array,NNUMMAX,2     !Damage initiation criteria array
*DIM,NARRAY_DE_INT,array,1          !Damage exceeded variable interface
*DIM,NARRAY_DE_SOFT,array,1         !Damage exceeded variable soft material
*DIM,NARRAY_MEAN,array,NNUMMAX,5    !Mean principal stress
*DIM,NARRAY_SOFT,array,NNUMMAX,3    !soft material principal stresses

CMSEL,s,soft_hard,node
*VGET,NMASK(1),node,1,nsel
CMSEL,s,Soft2,node
*VGET,NMASK_SOFT(1),node,1,nsel


*VMASK,NMASK(1)                                         !node array
*VFILL,NARRAY(1,1),ramp,1,1

*VMASK,NMASK(1)                                         !location array
*VGET,NARRAY_LOC(1,1),node,1,LOC,X
*VMASK,NMASK(1)
*VGET,NARRAY_LOC(1,2),node,1,LOC,Y
*VMASK,NMASK(1)
*VGET,NARRAY_LOC(1,3),node,1,LOC,Z

*VMASK,NMASK(1)                                         !stress array
*VGET,NARRAY_S(1,1),node,1,S,X
*VMASK,NMASK(1)
*VGET,NARRAY_S(1,2),node,1,S,Y
*VMASK,NMASK(1)
*VGET,NARRAY_S(1,3),node,1,S,Z
*VMASK,NMASK(1)
*VGET,NARRAY_S(1,4),node,1,S,XY
*VMASK,NMASK(1)
*VGET,NARRAY_S(1,5),node,1,S,YZ
*VMASK,NMASK(1)
*VGET,NARRAY_S(1,6),node,1,S,XZ

*VMASK,NMASK(1)                                         !principal stress array interface
*VGET,NARRAY_PR(1,1),node,1,S,1
*VMASK,NMASK(1)
*VGET,NARRAY_PR(1,2),node,1,S,2
*VMASK,NMASK(1)
*VGET,NARRAY_PR(1,3),node,1,S,3

*VFUN,NARRAY_EU,EULER,NARRAY_S                          !euler angles array

*VMASK,NMASK_SOFT(1)                                    !principal strain array soft material
*VGET,NARRAY_SOFT(1,1),node,1,EPTO,1
*VMASK,NMASK(1)
*VGET,NARRAY_SOFT(1,2),node,1,EPTO,2
*VMASK,NMASK(1)
*VGET,NARRAY_SOFT(1,3),node,1,EPTO,3
```

Figure C.2: Ansys APDL command snippet to calculate the critical interface stresses.

```
87
88
89  !##### Edge length #####
90  Length = 0
91  *VOPER,NARRAY_LOC(1,4),NARRAY_LOC(1,1),SUB,NARRAY_LOC(2,1)   !difference in x
92  *VFUN,NARRAY_LOC(1,4),PWR,NARRAY_LOC(1,4),2                  !difference in x squared
93  *VOPER,NARRAY_LOC(1,5),NARRAY_LOC(1,2),SUB,NARRAY_LOC(2,2)   !difference in y
94  *VFUN,NARRAY_LOC(1,5),PWR,NARRAY_LOC(1,5),2                  !difference in y squared
95  *VOPER,NARRAY_LOC(1,6),NARRAY_LOC(1,4),ADD,NARRAY_LOC(1,5)   !addition squared differences
96  *VFUN,NARRAY_LOC(1,6),SQRT,NARRAY_LOC(1,6)                   !square root --> length between nodes array
97  *VOPER,NARRAY_LOC(1,7),NARRAY_LOC(1,6),LT,0.6                !consider only values less then 0.6 mm
98  *VOPER,NARRAY_LOC(1,7),NARRAY_LOC(1,6),MULT,NARRAY_LOC(1,7)
99  *VMASK,NMASK(1)
100 *VSCFUN,Length,SUM,NARRAY_LOC(1,7)                           !total length
101
102 !##### Tangent Curve Vector #####
103 *VFUN,NARRAY_TAN,TANG,NARRAY_LOC                             !tangent curve vector arrays
104
105 !##### Principal Load Vector #####
106 *VOPER,NARRAY_EU(1,4),0.01745329251,MULT,NARRAY_EU(1,1)      !first principal stress load vector
107 *VFUN,NARRAY_PLV(1,1),COS,NARRAY_EU(1,4)                     !x-component of principal load vector
108 *VFUN,NARRAY_PLV(1,2),SIN,NARRAY_EU(1,4)                     !y-component of principal load vector
109 *VMASK,NMASK(1)
110 *VFILL,NARRAY_PLV(1,3),ramp,0,0
111
112 !##### Curve-Load Angle #####
113 *VABS,1,0,0,0                                               !absolute value of next result
114 *VOPER,NARRAY_ANG(1,1),NARRAY_TAN,DOT,NARRAY_PLV
115 *VFUN,NARRAY_ANG(1,1),ACOS,NARRAY_ANG(1,1)
116
117 !##### Principal-Von Mises load Angle #####
118 *VOPER,NARRAY_VM(1,1),1,MULT,NARRAY_PR(1,1)                  !Von Mises stress vector
119 *VOPER,NARRAY_VM(1,2),1,MULT,NARRAY_PR(1,2)
120 *VOPER,NARRAY_VM(1,3),1,MULT,NARRAY_PR(1,3)
121 *VFUN,NARRAY_VM(1,4),PWR,NARRAY_VM(1,1),2
122 *VFUN,NARRAY_VM(1,5),PWR,NARRAY_VM(1,2),2
123 *VOPER,NARRAY_VM(1,6),NARRAY_VM(1,4),ADD,NARRAY_VM(1,5)
124 *VFUN,NARRAY_VM(1,6),SQRT,NARRAY_VM(1,6)                     !VM vector length
125 *VOPER,NARRAY_PR1(1,1),1,MULT,NARRAY_PR(1,1)                 !first principal stress vector
126 *VOPER,NARRAY_PR1(1,2),0,MULT,NARRAY_PR(1,2)
127 *VOPER,NARRAY_PR1(1,3),0,MULT,NARRAY_PR(1,3)
128 *VOPER,NARRAY_VM(1,6),NARRAY_PR1(1,1),MULT,NARRAY_VM(1,6)   !VM length times principal length
129 *VABS,1,0,0,0                                               !absolute value of next result
130 *VOPER,NARRAY_ANG(1,2),NARRAY_PR1,DOT,NARRAY_VM             !absolute dot product principal-VM stress vectors
131 *VOPER,NARRAY_ANG(1,2),NARRAY_ANG(1,2),DIV,NARRAY_VM(1,6)   !dot product divided by lengths
132 *VFUN,NARRAY_ANG(1,2),ACOS,NARRAY_ANG(1,2)
133
134 !##### Curve-Von Mises load Angle #####
135 *VOPER,NARRAY_ANG(1,3),NARRAY_ANG(1,1),ADD,NARRAY_ANG(1,2)
136 *VABS,1,0,0,0                                               !absolute value of next result
137 *VFUN,NARRAY_ANG(1,3),COS,NARRAY_ANG(1,3)
138 *VFUN,NARRAY_ANG(1,3),ACOS,NARRAY_ANG(1,3)
139 *VOPER,NARRAY_ANG(1,3),57.2957795131,MULT,NARRAY_ANG(1,3)   !radians to degrees
140
141 !##### Damage Initiation Criteria #####
142 *VMASK,NMASK(1)
143 *VFILL,NARRAY_CRIT(1,1),ramp,ARG1,0                          !sigma mode I
144 *VMASK,NMASK(1)
145 *VFILL,NARRAY_CRIT(1,2),ramp,ARG2,0                          !sigma mode II
146 *VOPER,NARRAY_CRIT(1,3),NARRAY_ANG(1,3),DIV,90               !m
147 *VOPER,NARRAY_CRIT(1,4),1,SUB,NARRAY_CRIT(1,3)               !(1-m)
148 *VFUN,NARRAY_CRIT(1,1),PWR,NARRAY_CRIT(1,1),ARG3            !to the power alpha
149 *VFUN,NARRAY_CRIT(1,2),PWR,NARRAY_CRIT(1,2),ARG3            !to the power alpha
150 *VFUN,NARRAY_CRIT(1,3),PWR,NARRAY_CRIT(1,3),ARG3            !to the power alpha
151 *VFUN,NARRAY_CRIT(1,4),PWR,NARRAY_CRIT(1,4),ARG3            !to the power alpha
152 *VOPER,NARRAY_CRIT(1,5),NARRAY_CRIT(1,1),MULT,NARRAY_CRIT(1,2)
153 *VOPER,NARRAY_CRIT(1,6),NARRAY_CRIT(1,1),MULT,NARRAY_CRIT(1,4)
154 *VOPER,NARRAY_CRIT(1,7),NARRAY_CRIT(1,2),MULT,NARRAY_CRIT(1,3)
155 *VOPER,NARRAY_CRIT(1,8),NARRAY_CRIT(1,6),ADD,NARRAY_CRIT(1,7)
156 *VOPER,NARRAY_CRIT(1,9),NARRAY_CRIT(1,5),DIV,NARRAY_CRIT(1,8)
157 *VFUN,NARRAY_CRIT(1,10),PWR,NARRAY_CRIT(1,9),1/ARG3          !to the inverse power of alpha
158
159 !##### Performance index #####
160 Sigma_crit_tot = 0
161 *VOPER,NARRAY_CRIT(1,11),NARRAY_CRIT(1,10),MULT,NARRAY_LOC(1,7)
162 *VSCFUN,Sigma_crit_tot,SUM,NARRAY_CRIT(1,11)                 !total critical principal strain
163 Sigma_crit_tot = Sigma_crit_tot/Length                       !critical principal strain per unit contact length [MPa/mm]
164
165 *VOPER,NARRAY_DIC(1,1),NARRAY_PR(1,1),GT,NARRAY_CRIT(1,10)
166 *VSCFUN,NARRAY_DE_INT(1),MAX,NARRAY_DIC(1,1)
167
168 *VOPER,NARRAY_DIC(1,2),NARRAY_SOFT(1,1),GT,1.00              !critical value soft material strain
169 *VSCFUN,NARRAY_DE_SOFT(1),MAX,NARRAY_DIC(1,2)
170
171
172 !##### Data Export #####
173 *CFOPEN,Write_debug_pro,txt
174 *VWRITE
175 ('NODE',10x,'compare',10x,'PS1',10x,'Criteria')
176 *VMASK,NMASK(1)
177 *VWRITE,NARRAY(1,1),NARRAY_DIC(1,1),NARRAY_PR(1,1),NARRAY_CRIT(1,10)
178 (F10.6,t11,' ',F10.6,' ',F10.6,' ',F10.6)
179 *CFCLOS
180
181
182 PARSAV,all,parm_pro
183
184 ALLSEL
185 FINISH
186
187 /SOLU
188 ANTYPE,,restart,last,last,continue                           ! continue from most recent loadstep/substep.
189 *ENDIF
190
```

Figure C.3: Ansys APDL command snippet, continued.